Ocean Modelling 145 (2020) 101522

Contents lists available at ScienceDirect

Ocean Modelling

journal homepage: www.elsevier.com/locate/ocemod

Effect of oil plumes on upper-ocean radiative transfer — A numerical study

Shuolin Xiao, Di Yang *

Department of Mechanical Engineering, University of Houston, Houston, TX 77004, USA

ARTICLE INFO

Keywords:
Oil spill dispersion
Ocean optics
Turbulence
Wave

ABSTRACT

Oil plumes released from subsea blowouts can induce strong optical extinction effect and significantly affect radiative transfer in the ocean euphotic zone where photosynthesis occurs. In this paper, the effect of oil plumes on the ocean radiative transfer is studied numerically by modeling the dispersion of oil plume in the ocean mixed layer and the radiative transfer through the oil-contaminated seawater. Due to the interactions with flows in the ocean mixed layer, oil plumes of different droplet diameters exhibit considerable differences in plume size, shape and oil concentration. With the same volumetric release rate, plumes of large oil droplets exhibit highly intermittent local concentration in near-surface regions and cause strong but intermittent extinction effect over relatively small horizontal area; plumes of small oil droplets diffuse more smoothly over large horizontal and vertical extensions, resulting in significant overall extinction effect to the radiative transfer in the ocean euphotic zone.

1. Introduction

Crude oil, as indicated by its dark color, is a strong absorber of light when spilled into the upper ocean (Otremba, 2007). In the aftermath of a large-scale offshore oil spill, such as the 2010 *Deepwater Horizon* accident, spilled crude oil can spread over a large horizontal area in the upper ocean and last for long time before being restored or biodegraded, inducing significant impact on the ocean ecosystem (Atlas and Hazen, 2011; Camilli et al., 2010; Hazen et al., 2010). Surface oil slicks and suspended oil droplets in the euphotic zone can block light from penetrating into subsurface region where phytoplankton live (Kirk, 2011), threatening the ocean ecosystem from the origin of its food chain by significantly reducing the rate of photosynthesis. On the other hand, ultraviolet light can alter (degrade) oil in the process of photo-degradation, which can produce some byproducts that can be more toxic than the source oil (King et al., 2014; Radović et al., 2014; Ray et al., 2014; Bacosa et al., 2015). Improved knowledge on the light penetration in oil-contaminated seawater can help obtain a more accurate estimation of the photo-degradation rate than using the normal light penetration profiles obtained based on the natural ocean condition. Recent report by Lay et al. (2015) based on the field measurement data obtained during the *Deepwater Horizon* oil spill incident has confirmed the noticeable effect of spilled crude oil on the vertical variation of incident ultraviolet radiation and extinction coefficients in the northern Gulf of Mexico. Thus understanding the oil-induced effects on the oceanic radiative transfer is crucial for accurately modeling the ocean ecosystem evolution in the wake of a large offshore oil spill.

Suspended crude oil droplets affect the local seawater's inherent optical properties (IOPs) (i.e. the light absorption and scattering coefficients), which depend on the local droplet number density, droplet size, and oil type (Otremba and Król, 2002; Król et al., 2006; Otremba, 2007; Rudź et al., 2013). The dispersion of oil droplets and other buoyant particles in the euphotic zone is actively driven by various physical processes induced by atmospheric forcing, e.g., shear-induced turbulence, sea-surface waves, Langmuir circulations, Ekman transport, thermal convection, etc. (Edson et al., 2007; Sullivan and McWilliams, 2010; Özgökmen et al., 2012; D'Asaro, 2014; Kukulka et al., 2016). These effects continuously mix the very upper tens of meters of the ocean to form the ocean mixed layer (OML), which can also cause considerable dilution of the oil droplet plume by horizontal and vertical mixing (see e.g., McWilliams and Sullivan, 2000; Yang et al., 2015). On the other hand, the buoyancy of the oil droplets acts as a resistant force to the mixing effects generated by the oceanic flows and can cause inhibition of oil plume dilution under certain conditions (Yang et al., 2014a).

In recent years, the continuous growth of computer power has made high-fidelity computational models feasible for tackling the complex ocean processes. Particularly, large-eddy simulation (LES) based on the Craik–Leibovich (CL) equation (Leibovich, 1983) has proven to be a useful tool for providing insights of fine-scale oceanic flows and transport phenomena (Skyllingstad and Denbo, 1995; McWilliams et al., 1997; Li et al., 2005; Noh et al., 2006; Harcourt and D'Asaro, 2008; Grant and Belcher, 2009; Kukulka et al., 2009; Li and Fox-Kemper, 2017). Using the LES method, several recent studies have been able to

* Corresponding author.
E-mail address: diyang@uh.edu (D. Yang).

https://doi.org/10.1016/j.ocemod.2019.101522
Received 21 February 2019; Received in revised form 30 September 2019; Accepted 6 November 2019
Available online 15 November 2019

shed light on the detailed three-dimensional dispersion processes of oil plumes in the OML under various conditions (Yang et al., 2014a, 2015; Chor et al., 2018a,b). In particular, under wind and wave dominant conditions, plumes of oil droplets are found to be strongly affected by Langmuir circulations and shear-induced turbulence, and exhibit various types of surface patterns with different dilution levels, ranging from highly intermittent surface streaks for large oil droplets to smoothly diffused plumes for small oil droplets (Yang et al., 2014a, 2015). Under convection dominant conditions, buoyant materials show strong preferential concentration in surface convergence regions generated by convective cells; in addition, highly buoyant particles (e.g., large oil droplets) can also be affected by a secondary effect induced by some persistent surface vortices in the turbulent flow field that collect and cluster these particles into vorticity-dominant surface regions (Chor et al., 2018a).

Due to the considerable spatial variation of oil droplet concentration caused by these aforementioned flow-induced transport phenomena in the OML, the IOPs of the oil-contaminated seawater can also exhibit complex spatial variations that can strongly affect the variation of light intensity in the euphotic zone, which is a crucial information for modeling the light variation due to oil spill but has not been well understood up to date. Simple one-dimensional downward irradiance models (e.g. Woźniak et al., 2003; Lee et al., 2005; Woźniak and Dera, 2007) require the information about the diffuse attenuation coefficient, which is an apparent optical property of the water body and is not available from the literature for the ocean contaminated by oil plumes with complex spatial variations. This directly motivates the current study. With the detailed three-dimensional flow field information in hand, the oceanic light field can be efficiently modeled by solving the radiative transfer equation using the Monte Carlo simulation (MCS) method (Kirk, 1981a,b; Gordon, 1985). Simulations based on the MCS method can capture the three-dimensional radiative transfer in dynamic ocean covered by wind-generated sea-surface waves (You et al., 2009; Xu et al., 2011). The combination of LES and MCS methods has been demonstrated to provide valuable insights for understanding the complex effects of ocean turbulence on its optical properties (Xu et al., 2012). The effects of particles on the radiative transfer can also be included in the MCS method using the Mie theory (e.g. Plass and Kattawar, 1972; Wang and Wang, 2002).

In this study, we utilize these recent advancements in computational models to establish a numerical modeling framework for simulating the radiative transfer in the ocean euphotic zone contaminated by plumes of suspended crude oil droplets. We perform two sets of numerical experiments corresponding to two representative OML flow conditions: (1) wind/wave dominant condition with shear-generated turbulence and wave-induced Langmuir circulations, and (2) convection dominant condition with thermal convective cells. Because the oil droplet size plays a crucial role in determining both the dynamic response of the oil plume to the OML flows (Yang et al., 2014a, 2015) and the light absorption/scattering (Mie, 1908; Otremba and Król, 2002; Otremba, 2007), for each OML condition we consider three different oil droplet diameters. All together, these simulation cases allow us to cover a variety of oil plume patterns with different levels of horizontal and vertical dilutions, from which the effect of oil contamination on oceanic radiative transfer is studied. Fig. 1 illustrates the problem configuration and some representative results for the effect of flow and oil field on the radiative transfer.

This paper is organized as follows. Details of the computational models used in this work are reported in Section 2. Section 3 shows the simulation and statistical analysis results. Finally, conclusions are given in Section 4.

2. Numerical models

2.1. Highlight of modeling strategy

Radiative transfer in natural seawater is affected by the sea-surface geometry and seawater properties underneath the surface (e.g., temperature, salinity, suspended particulate matter, colored dissolved organic matter, etc.) (Mobley, 1994; Kirk, 2011). In the case of an offshore oil spill incident, the presence of suspended oil droplets further complicates the radiative transfer process and causes considerable variation to the subsurface light field.

Note that the essential physical processes that affect the light field (i.e. wave oscillation, turbulence mixing and transport, and photon propagation) occur at very different time scales. For example, the ocean waves oscillate at the periods of $O(0.1) \sim O(10)$ seconds depending on the wavelength. The surface oil plumes evolve at the time scale of minutes for small-scale features and hours for large-scale patterns. A photon's lifetime when propagating in the upper ocean is on the order of $O(0.001) \sim O(0.1)$ microseconds depending on the penetration depth. The considerable time-scale separation and significant differences in the details of the physical processes impose great challenges. In this study we adopted a suite of numerical models that were designed for capturing different aspects of this complex physical problem, and combined their strengths to tackle the problem. The overall modeling strategy is highlighted below:

(i) The instantaneous sea-surface wave field is simulated using a high-order spectral (HOS) method (Dommermuth and Yue, 1987), which provides the geometry of the air–water interface for modeling the light refraction at the sea surface based on Snell's law and Fresnel's equations (You et al., 2009; Xu et al., 2011). (See details in Section 2.2 and Appendix A.)

(ii) Underneath the sea surface, the OML flow field is simulated using a LES model (Yang et al., 2014a), which models the oceanic flow structures (e.g. shear turbulence, Langmuir circulations, convective cells, etc.) generated by sea-surface wind shear stress, surface heat flux, and wave-induced Stokes drift. This LES model is based on the widely used Craik–Leibovich equation, in which the accumulated effect of sea-surface waves on the turbulence and material transport is modeled based on the wave-induced Stokes drift current (Leibovich, 1983). (See details in Section 2.3.)

(iii) In the ocean column, the transport of crude oil droplets is modeled using an Eulerian–Eulerian LES method (Yang et al., 2014a, 2015), in which the evolution of the concentration field of the oil droplets is simulated by a finite-volume LES model and is coupled with the LES model for oceanic flow described in (ii). (See details in Section 2.3.)

(iv) Based on the instantaneous sea-surface wave geometry obtained from (i) and the instantaneous oil droplet concentration obtained from (iii), the seawater IOPs are modeled and the radiative transfer in the euphotic zone is simulated by a MCS model. This model can capture the effects of suspended oil droplets on the absorption and scattering of photons as they propagate through the mixture of seawater and oil droplets. (See details in Section 2.4 and Appendix B.)

Each of these above models has proven track record for modeling their corresponding physical processes in various applications, and their details are presented in the next several subsections. Fig. 1 shows a representative example of the simulation results obtained by this set of numerical models.

Because the physical processes involved in the current problem are complicated and occur over a wide range of time and length scales, it is impractical to perform the simulations with each of the above models fully coupled in a two-way dynamic coupling manner. Instead, in the current study the hydrodynamic models (i)–(iii) are used as precursor simulators to provide the required flow field data for the MCS model (iv) to simulate the radiative transfer in the oil-contaminated seawater. Among the three hydrodynamic models (i)–(iii), the two LES models (ii) and (iii) are dynamically coupled to simulate the oil plume dispersion in the upper ocean in a wave-averaged but turbulence-resolved manner. As explained below in Section 2.3, the coupled LES models account for the accumulated effect of sea-surface waves on the oil transport, but do not model the instantaneous waves explicitly. The HOS model (i) uses

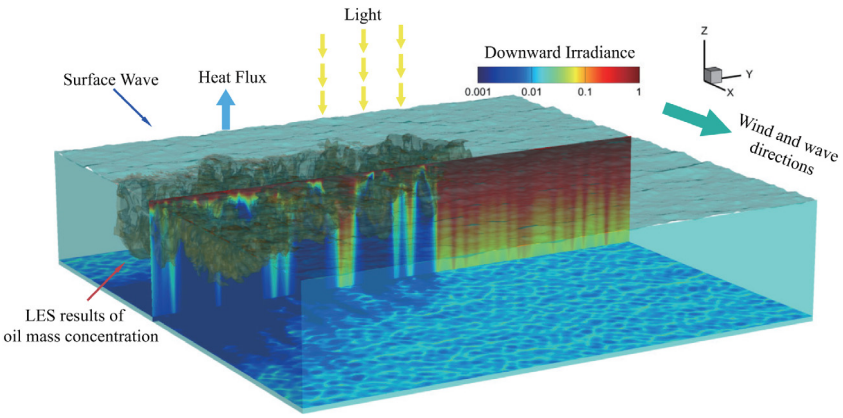

Fig. 1. Overview of the numerical modeling results for the effect of dispersed oil plume on the upper-ocean radiative transfer. The oil plume is visualized using the iso-surfaces (in brown color) of oil droplet concentration. Contours of the downward irradiance are shown on the vertical plane cutting through the oil plume as well as on the bottom plane of the plotted simulation domain.

identical wave spectra as in the LES model to provide the corresponding wave surface geometry. The combination of the surface waves and the subsurface oil concentration field provides a synthetic upper-ocean field for modeling the radiative transfer process. Details of each models are discussed below in Sections 2.2–2.4 as well as in Appendices A and B.

2.2. High-order spectral simulation of sea-surface waves

When light strikes on the sea surface, it first interacts with the air–water interface curved due to waves. In this study, we adopt the widely used high-order spectral method to simulate instantaneous sea-surface waves. The HOS method models the wave motions based on the potential flow theory, in which the wave orbital velocity satisfies $\mathbf{u} = \nabla\Phi$, where Φ is the velocity potential. In the water body, the wave-induced flow motions satisfy the continuity equation $\nabla^2\Phi = 0$. On the sea surface, the wave satisfies both the kinematic and dynamic free-surface boundary conditions, which can be defined precisely at the instantaneous wave surface $z = \eta(x, y, t)$ using Zakharov's equations (Zakharov, 1968),

$$\frac{\partial\eta}{\partial t} + \hat{\nabla}\eta\cdot\hat{\nabla}\Phi^s + \left(1+|\hat{\nabla}\eta|^2\right)\frac{\partial}{\partial z}\Phi(x,y,\eta,t) = 0 \quad \text{at } z=\eta, \tag{1}$$

$$\frac{\partial\Phi^s}{\partial t} + g\eta + \frac{|\hat{\nabla}\Phi^s|^2}{2} - \frac{1}{2}\left(1+|\hat{\nabla}\eta|^2\right)\left[\frac{\partial}{\partial z}\Phi(x,y,\eta,t)\right]^2 = 0 \quad \text{at } z=\eta. \tag{2}$$

Here, η is the instantaneous wave surface elevation, $\Phi^s = \Phi|_{z=\eta}$ is the surface potential, and $\hat{\nabla} = (\partial/\partial x, \partial/\partial y)$ is the horizontal gradient.

For fast numerical simulation, the continuity equation and boundary conditions (1) and (2) are rewritten into series of discretized modes using perturbation method and eigenfunction expansion following Dommermuth and Yue (1987) (also see Mei et al., 2005), and are solved numerically using Fourier series based pseudo-spectral method. Additional details of the current HOS model are given in Appendix A. The HOS method has been successfully applied to a variety of different ocean surface wave problems in recent years (see e.g., Liu and Yue, 1998; Tanaka, 2001; Alam et al., 2010; Goullet and Choi, 2011; Yang and Shen, 2011; Yang et al., 2013, 2014b,c). Fig. 2(a) shows a sample result of sea-surface wave field simulated using the current HOS model.

2.3. Large-eddy simulation of turbulent flows and oil plume transport in ocean mixed layer

To efficiently simulate the Langmuir circulations and shear/convection driven turbulent flows in the ocean mixed layer and the corresponding oil plume transport, we employ a LES model that consists of a pseudo-spectral/finite-difference flow solver based on the CL equation and a finite-volume oil transport solver (Chamecki et al., 2008; Yang et al., 2014a). This LES model has been successfully applied to simulate oil and buoyant particle dispersion in OML in several recent studies (Yang et al., 2014a, 2015; Chen et al., 2016; Chor et al., 2018a,b). In this model, the OML flows are governed by the filtered continuity equation and CL equation,

$$\nabla\cdot\tilde{\mathbf{u}} = 0\,, \tag{3}$$

$$\frac{\mathrm{D}\tilde{\mathbf{u}}}{\mathrm{D}t} = -\frac{1}{\rho_0}\nabla\tilde{P} - f_c\mathbf{e}_3\times(\tilde{\mathbf{u}}+\mathbf{u}_s) + \mathbf{u}_s\times\tilde{\boldsymbol{\omega}} - \nabla\cdot\boldsymbol{\tau}^d + \left(1-\frac{\tilde{\rho}}{\rho_0}\right)g\mathbf{e}_3\,. \tag{4}$$

Here, tilde denotes a variable resolved on the LES grid, $\mathbf{u}$ is the fluid velocity vector, $\mathrm{D}/\mathrm{D}t = \left(\partial/\partial t + \tilde{\mathbf{u}}\cdot\nabla\right)$ is the material derivative, ρ_0 is the reference seawater density, $\tilde{\rho}$ is the resolved local seawater density, P is the modified pressure, g is the gravitational acceleration, $\mathbf{e}_3$ is the unit vector in the vertical direction, f_c is the Coriolis frequency, $\mathbf{u}_s$ is the wave-induced Stokes drift velocity, $\boldsymbol{\omega} = \nabla\times\mathbf{u}$ is the vorticity, and $\boldsymbol{\tau} = (\widetilde{\mathbf{u}\mathbf{u}} - \tilde{\mathbf{u}}\tilde{\mathbf{u}})$ is the subgrid-scale (SGS) stress tensor with $\mathrm{tr}(\boldsymbol{\tau})$ being its trace and $\boldsymbol{\tau}^d = \boldsymbol{\tau} - [\mathrm{tr}(\boldsymbol{\tau})/3]\mathbf{I}$ being its deviatoric part, and $\mathbf{I}$ is the identity tensor. The first four terms on the right-hand side of Eq. (4) are pressure gradient force, Coriolis force, the vortex force due to Stokes drift representing the phase-averaged effects of surface gravity waves on the mean flow and turbulence, and the SGS term representing the effect of unresolved fluid motions below LES grid scale. Details for modeling the Stokes drift current $\mathbf{u}_s(z)$ are given further below.

The last term in Eq. (4) is the buoyancy force due to density variation, which is formed based on the Boussinesq approximation (see e.g., McWilliams et al., 1997; Özgökmen et al., 2011). The buoyancy force induced by the oil droplets is neglected due to the low released rate considered in this study and the low local oil concentration after turbulence-induced dilution. Following previous LES studies (e.g., McWilliams et al., 1997; Polton et al., 2008; Kukulka et al., 2010; Yang et al., 2014a, 2015), we assume the seawater density satisfies a linear equation of state, i.e. $\tilde{\rho} = \rho_0\left[1-\alpha_t(\tilde{\Theta}-\Theta_0)\right]$, where $\alpha_t = 2\times10^{-4}\ \mathrm{K}^{-1}$ is the thermal expansion coefficient, $\tilde{\Theta}$ is the resolved potential temperature, and Θ_0 is the reference temperature corresponding to ρ_0. The variation of the potential temperature field is computed by solving a filtered convection–diffusion equation

$$\frac{\mathrm{D}\tilde{\Theta}}{\mathrm{D}t} = -\mathbf{u}_s\cdot\nabla\tilde{\Theta} - \nabla\cdot\boldsymbol{\pi}_t\,, \tag{5}$$

where $\boldsymbol{\pi}_t = (\widetilde{\mathbf{u}\Theta} - \tilde{\mathbf{u}}\tilde{\Theta})$ is the SGS heat flux. The transport of oil plumes in OML flows is simulated using an Eulerian approach (Chamecki et al., 2008; Yang et al., 2014a). Oil droplets of the same diameter d are considered as one species, and their instantaneous distribution is represented by a continuous Eulerian mass concentration field $C(\mathbf{x}, t)$. The evolution of C is governed by the filtered transport equation

$$\frac{\partial\tilde{C}}{\partial t} + \nabla\cdot\left(\tilde{\mathbf{v}}\tilde{C}\right) = -\nabla\cdot\boldsymbol{\pi}_c + Q_s\,, \tag{6}$$

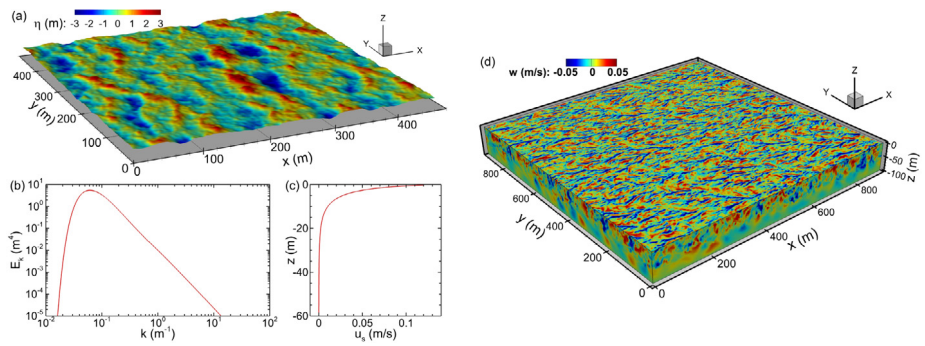

Fig. 2. Sample results for a broadband wave field under 10 m/s wind: (a) instantaneous surface waves obtained by the HOS model; (b) empirical wave spectrum from Donelan and Pierson (1987); (c) Stokes drift current profile calculated based on the integral Eq. (9); (d) sample result of Langmuir circulations obtained using the LES model based on the Stokes drift in (c). The color contours in (a) indicate the instantaneous wave elevation on the sea surface. The contours in (d) indicate the instantaneous vertical velocity, and the horizontal plane shown in the figure is chosen at the depth of 5 m beneath the mean sea surface level.

where $\boldsymbol{\pi}_c = (\widetilde{\mathbf{u}C} - \widetilde{\mathbf{u}}\widetilde{C})$ is the SGS oil concentration flux, Q_s is a source term for subsurface release of the oil droplets, and $\widetilde{\mathbf{v}}$ is the resolved Lagrangian transport velocity of the oil droplets, which is modeled as (Ferry and Balachandar, 2001; Yang et al., 2014a, 2015; Chen et al., 2016)

$$\widetilde{\mathbf{v}} = \widetilde{\mathbf{u}} + \mathbf{u}_s + w_r\mathbf{e}_3 + (R-1)T_d\left(\frac{\mathrm{D}\widetilde{\mathbf{u}}}{\mathrm{D}t} + \nabla\cdot\boldsymbol{\tau}\right) + \mathcal{O}(T_d^{3/2}) . \tag{7}$$

Here, w_r is the droplet rise velocity (relative to the surrounding fluid) due to the balance of buoyancy, gravity and Stokes drag, which is modeled as (Balachandar and Eaton, 2010; Yang et al., 2016)

$$w_r = \begin{cases} w_{r,S} & \mathrm{Re}_d < 0.2, \\ w_{r,S}\left(1 + 0.15\mathrm{Re}_d^{0.687}\right)^{-1}, & 0.2 < \mathrm{Re}_d < 750, \end{cases} \tag{8}$$

where $w_{r,S} = (\rho_0 - \rho_d)gd^2/(18\mu)$ is the droplet rise velocity given by Stokes' law, ρ_d is the oil density, $\mathrm{Re}_d = \rho_0 w_r d/\mu$ is the particle Reynolds number, and μ is the dynamic viscosity of the seawater. The first three terms on the right-hand side of Eq. (7) represent the dominant effects acting on buoyant particles in OML flows. The fourth term on the right-hand side of Eq. (7) represents the additional effects due to added mass and SGS fluid stress force, where $R = 3\rho_0/\left(2\rho_d + \rho_0\right)$ is the density ratio parameter and $T_d = w_r/[(R-1)g]$ is the droplet response time scale (Yang et al., 2015, 2016).

In order to solve Eqs. (4)–(6), proper turbulence closures are required for the SGS terms $\boldsymbol{\tau}$, $\boldsymbol{\pi}_t$ and $\boldsymbol{\pi}_c$. In the current model, the SGS stress tensor $\boldsymbol{\tau}$ is parameterized using the Lilly–Smagorinsky eddy-viscosity model (Smagorinsky, 1963; Lilly), i.e. $\boldsymbol{\tau} = -2\nu_\tau\widetilde{\mathbf{S}} = -2(c_s\Delta)^2|\widetilde{\mathbf{S}}|\widetilde{\mathbf{S}}$, where $\widetilde{\mathbf{S}} = [\nabla\widetilde{\mathbf{u}} + (\nabla\widetilde{\mathbf{u}})^T]/2$ is the resolved strain rate tensor, ν_τ is the SGS eddy viscosity, Δ is the LES grid (filter) scale, and c_s is the Smagorinsky coefficient. The instantaneous and local value of c_s is determined dynamically during the simulation using the Lagrangian-averaged scale-dependent dynamic model (Bou-Zeid et al., 2005). With the SGS eddy viscosity modeled as $\nu_\tau = (c_s\Delta)^2|\widetilde{\mathbf{S}}|$, the SGS heat flux $\boldsymbol{\pi}_t$ and oil mass flux $\boldsymbol{\pi}_c$ are then parameterized as $\boldsymbol{\pi}_t = -(\nu_\tau/\mathrm{Pr}_\tau)\nabla\widetilde{\Theta}$ and $\boldsymbol{\pi}_c = -(\nu_\tau/\mathrm{Sc}_\tau)\nabla\widetilde{C}$ based on constant turbulent Prandtl number $\mathrm{Pr}_\tau = 0.4$ and Schmidt number $\mathrm{Sc}_\tau = 0.4$ (Antonopoulos-Domis, 1981; Moeng, 1984; Mason, 1989; Sullivan et al., 1994; Kumar et al., 2006; Chamecki et al., 2009; Yang et al., 2014a, 2015). Note that for the simplification of the model, the temperature changes of the seawater and oil droplets due to light absorption are not considered in this study. The oil droplets and the surrounding seawater are assumed to be in thermal equilibrium state, so that the heat exchange between them is also omitted in Eq. (5).

In this study, we consider the typical open-sea condition such that the sea surface is covered by a broadband wind-generated surface wave field with a directional spectrum $S(k,\alpha)$, where $k = 2\pi/\lambda$ is the wavenumber, λ is the wavelength, α is the inclination angle between the wave propagation direction and the mean wind direction. Note that because the CL equation (4) models the accumulated effect of surface waves on the shear-driven turbulence in a wave phase-averaged context, the instantaneous sea-surface motions are not included in the simulation. Consistent with the CL modeling framework, the top boundary of the LES domain is modeled as a rigid flat surface with an imposed mean shear stress in the downwind direction (i.e. the x-direction in this study), and the fluctuating components of the horizontal velocity components satisfy the free-slip condition at this top boundary. The averaged wave effect is taken into account via the Stokes drift current. Following McWilliams and Restrepo (1999) (also see e.g. Harcourt and D'Asaro, 2008; Webb and Fox-Kemper, 2011; Li and Fox-Kemper, 2017), the leading-order approximation of the corresponding Stokes drift of such broadband sea-surface wave field can be calculated as

$$\mathbf{u}_s(z) = 2\sqrt{g}\int_0^\infty\int_{-\pi}^{\pi}\left(\cos\alpha\,\mathbf{e}_1 + \sin\alpha\,\mathbf{e}_2\right)k^{2.5}S(k,\alpha)\exp(2kz)\,\mathrm{d}\alpha\,\mathrm{d}k, \tag{9}$$

where $\mathbf{e}_1$ and $\mathbf{e}_2$ are the unit vectors in the x and y directions, respectively. In the simulations, the wave spectrum $S(k,\alpha)$ is prescribed based on the widely used empirical spectrum obtained by Donelan and Pierson (1987) based on field measurement data, and the Stokes drift $\mathbf{u}_s$ calculated by Eq. (9) is used in the LES model equations (4), (5) and (7) to simulate the OML flows. Fig. 2 shows some sample OML flow results obtained by this LES model.

2.4. Monte Carlo simulation for radiative transfer

The light transport in the ocean euphotic zone is governed by the radiative transfer equation (RTE) (Mobley, 1994; Xu and Yue, 2014), which can be simulated efficiently by the Monte Carlo simulation method (Kirk, 1981a,b). As illustrated in Fig. 3, the MCS method models the scattering and absorption events of photons as they travel in the seawater (i.e., a physical representation for the Neumann series of the RTE), which are controlled by the absorption coefficient a, scattering coefficient b, beam attenuation coefficient $c = a + b$, and scattering phase function $\mathscr{B}$. By tracing and calculating the summation of the scatterings and absorptions of many photons, the oceanic light field can be modeled. MCS method has been widely used for studying oceanic radiative transfer (see e.g., Kirk, 1981a,b; Gordon, 1985; Xu et al., 2011, 2012; Xu and Yue, 2014).

A general guidance of the MCS method can be found in Leathers et al. (2004). Additional details of the current MCS model are given in Appendix B. Details on modeling a, b and $\mathscr{B}$ for oil-contaminated seawater are also given in Appendix B. For simplification, in the current MCS model a "black sky" approximation is made such that the light absorption and scattering caused by the atmosphere are neglected. Consequently, a photon packet can be initialized right above the sea surface. Here, we summarize the key procedure of the MCS method used in this study as illustrated in Fig. 3:

(1) A photon packet with initial energy E_i is launched at a random location in the air right above the ocean surface, and travel towards the surface with an incident angle γ_i.

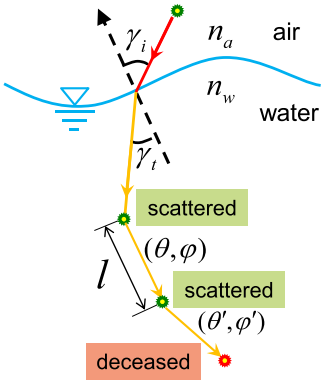

Fig. 3. Sketch of Monte Carlo simulation for radiative transfer.

(2) The photon packet passes through the air–water interface with a transmitted angle γ_t and energy E_t based on the Fresnel equations and the refraction indices of air (n_a) and water (n_w).
(3) When a photon packet travels through the oil-contaminated seawater, it experiences a medium with spatial variation of IOPs. To determine the optical pathlength l of the photon packet in this highly nonhomogeneous medium, the multi-stepped approach used by Wang et al. (1995) is adopted in the current MCS. In particular, the total pathlength is given by $l = \sum l_i$ with the sub-step pathlength l_i being determined by the equation $\sum l_i c_i = -\ln q_1$, where c_i is the local LES cell-averaged beam attenuation coefficient for the ith sub-step and q_1 is a random number within $[0, 1]$. In the simulation, the photon packet travels over the optical pathlength l with spatially varying c along its current travel direction described by (θ, φ), where θ and φ are the polar angle and azimuthal angle of the path, respectively.
(4) After traveling over l, a random number $q_2 \in [0, 1]$ is generated and compared with the single-scattering albedo $\omega_0 = b/c$. If $q_2 \le \omega_0$, the photon packet changes the traveling direction due to scattering, and a new set of angles (θ', φ') are determined based on the scattering phase function $\mathscr{B}$, and steps (3) and (4) are repeated; otherwise, the photon packet is deceased due to absorption, and a new photon packet is initialized and traced in the simulation by repeating steps (1)–(4).

Fig. 4 shows a sample result for the radiative transfer of 500 nm wavelength light in clean seawater underneath a surface wave field obtained from the current MCS model. In this MCS test case, the inherent optical properties of the seawater for the 500 nm light are set to be $a = 0.0257$ m^{-1}, $b = 0.0029$ m^{-1}, and $c = a + b = 0.0286$ m^{-1} (Smith and Baker, 1981). There were totally 5×10^{10} photon packets launched and tracked. As shown in the figure, the typical "swimming pool" effect associated with wave-induced light focusing is clearly visualized from the contours of the downward irradiance E_d at two representative depths (Fig. 4(b) and (c)). The local downward irradiance is calculated as (Xu et al., 2012)

$$E_d(x, y, z) = \int_0^{2\pi} \int_0^{\pi/2} I(x, y, z; \theta, \varphi) |\cos\theta| \sin\theta \, \mathrm{d}\theta \, \mathrm{d}\varphi, \tag{10}$$

where $I(x, y, z; \theta, \varphi)$ is the local radiance obtained from the MCS model. The MCS result also captures the depth-dependent decay of the horizontally averaged downward irradiance $\langle E_d \rangle$. Note that the vertical attenuation of the downward irradiance can be expressed in the form of an exponential decay function $\langle E_d \rangle = \langle E_{d,1} \rangle \exp[K_d(z - z_1)]$, where $\langle E_{d,1} \rangle$ is the average downward irradiance at the reference level $z_1 = -1$ m and K_d is the diffuse attenuation coefficient (Kirk, 2011). For this test case, $K_d = 0.0271$ m^{-1} (Smith and Baker, 1981). Fig. 4(d) shows good agreement between the MCS result and the exponential decay profile. Additional validations for the MCS model can be found in Appendix B.

3. Results

3.1. Problem setup

The upper-ocean boundary layer is a highly dynamic system, and it is nearly impossible to include all effects in a single modeling framework. To capture the detailed spatial variation of the light field, we choose to focus on small-scale effects (relative to submesoscale ocean eddies). As shown in Fig. 1, we consider the oil dispersion in the OML and the resulted light field variation under the influences of shear-induced turbulence, Langmuir circulations, sea-surface waves, and thermal convections. We consider two different sea-surface forcing conditions corresponding to shear-dominant and convection-dominant conditions. In the shear-dominant case, a constant wind shear stress $\tau_w = 0.168$ N m^{-2} is applied in the x-direction, which corresponds to a wind speed $U_{10} = 10$ m/s (measured at 10 m height) and a friction velocity $u_* = 1.28$ cm/s in water based on empirical parameterization (Donelan, 1982). A weak heat flux of $Q = -15.5$ W m^{-2} (out of the ocean) is imposed at the surface to help spin-up the flow (McWilliams et al., 1997; Yang et al., 2014a, 2015). Under this condition, the OML flow is dominated by the three-dimensional turbulence generated by the wind-induced shear and the coherent Langmuir circulation cells generated by wave–turbulence interaction (the wave condition is discussed further below). In the rest of this paper, we refer to this flow condition as LC. In the convection-dominant case we apply a weaker wind stress $\tau_w = 0.036$ N m^{-2} (corresponding to wind speed $U_{10} = 5$ m/s and friction velocity $u_* = 0.59$ cm/s in water) and a stronger surface heat flux of $Q = -207.0$ W m^{-2}. Under this condition, the convective cells generated by the thermal convection are the dominant flow structures, and hereinafter we refer to this condition as CC. For both flow conditions, we set the Coriolis frequency to be $f_c = 7 \times 10^{-5}$ s^{-1}, corresponding to a latitude of 28.7°N. Note that the surface heat flux imposed in the LES represents the combined effect of various surface heat transfer processes (e.g., convection, radiation and evaporation) (Edson et al., 2007), which are typically not modeled explicitly in the LES model based on the CL equation. Nevertheless, the surface wind stress and heat flux conditions considered in this study fall in the range of the parameters considered in previous LES studies of OML flows (e.g., McWilliams et al., 1997; Harcourt and D'Asaro, 2008; Mensa et al., 2015; Yang et al., 2015; Chor et al., 2018b).

For both flow conditions, we assume the sea-surface wave field is in equilibrium with the wind forcing. We adopt a widely used empirical broadband wave spectrum parameterization (Donelan and Pierson, 1987). The wavelengths at the spectrum peak are $\lambda_p = 92.2$ m for LC and 23.1 m for CC, and the corresponding wave periods are $T_p = 7.69$ s and 3.85 s, respectively. Based on these empirical spectra, for each flow condition a three-dimensional broadband wave field is constructed and used as the initial condition for the HOS model to simulate the instantaneous sea-surface waves. Underneath the sea surface, we use a computational domain of 922 m long and wide and 100 m deep to simulate the oil dispersion in OML using LES with $384 \times 384 \times 256$ computational grid points. The flow field is well mixed in the top half of the domain corresponding to an OML depth $z_i = 50$ m, and stably stratified further below with a temperature gradient $\mathrm{d}\Theta/\mathrm{d}z = 0.01$ K m^{-1}. For the broadband wave conditions considered in this study, the corresponding Stokes drift currents are calculated by integrating the wave spectra (McWilliams and Restrepo, 1999; Harcourt and D'Asaro, 2008; Webb and Fox-Kemper, 2011; Li and Fox-Kemper, 2017). The corresponding turbulent Langmuir number is about the same for both the LC and CC conditions, $La_t = \sqrt{u_*/u_{s,0}} = 0.3$, where u_* is the friction velocity in the water caused by the wind shear and $u_{s,0}$ is the magnitude of the wave-induced Stokes drift velocity at the mean water surface level (McWilliams et al., 1997).

Following recent LES studies on oil plume dispersion in OML (e.g., Yang et al., 2014a, 2015), we use the reference seawater density $\rho_0 = 1031.0$ kg/m^3 and viscosity $\mu_f = 1.08 \times 10^{-3}$ kg/(m s), and the oil

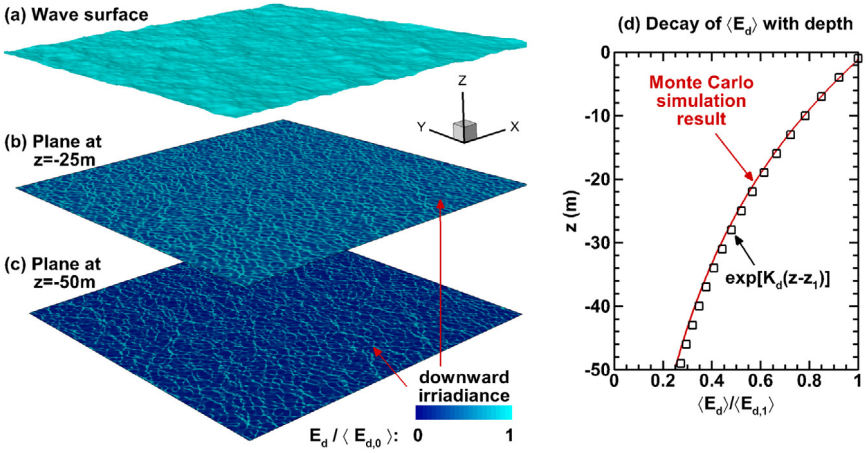

Fig. 4. Sample result for MCS of 500 nm wavelength light transfer in clean seawater. The left panel shows the downward irradiance E_d underneath a sea-surface wave field. The values are normalized by the averaged downward irradiance $\langle E_{d,0}\rangle$ of the incident light at the sea surface. The right panel shows vertical decay of plane-averaged downward irradiance $\langle E_d\rangle(z)$. The profile is normalized by its value at 1 m depth, $\langle E_{d,1}\rangle$. In this sample case, the inherent optical properties of the seawater are $(a, b) = (0.0257, 0.0029)$ m^{-1} and diffuse attenuation coefficient is $K_d = 0.0271$ m^{-1} (Smith and Baker, 1981). The incident light is directed vertically. The horizontal domain size is 512 m × 512 m, and the vertical distances between the three planes in (a)–(c) are artificially increased to avoid blocking the view of the results.

density $\rho_d = 859.9$ kg/m^3. For each flow condition, we consider three different cases differentiated by the droplet diameter, i.e. $d = 0.27$, 0.42 and 0.70 mm. These droplet diameters fall into the small size range (i.e. typically $d \leq 1$ mm) so that the droplets can be assumed to have spherical shape (Clift et al., 1978; Zheng and Yapa, 2000), and are within the range of possible droplet size distributions reported for offshore oil spills (Li et al., 2017). For each case, a monodisperse oil plume with the same droplet size is released from a localized source at the 75 m depth with a low mass release rate of $Q_s = 10$ kg/s. In this way, the oil plume in each case models a near-surface sub-plume of oil droplets with similar size originated from a deep-water release (note that the sub-plumes with different droplet sizes would rise along different paths in the OML due to the differences in their rise velocities) (Yang et al., 2015). The resulting oil concentration in the surface plume is found to be within the range of the concentration levels obtained from simulations based on the realistic scale blowout rate from the wellhead (Chen et al., 2018). The local oil concentrations obtained from the LES runs are also found to be at a level that induce negligible buoyancy effect to the two OML flow conditions considered in this study.

In the MCS, the incident light is directed vertically downward. The IOPs induced by naturally existing substances in the seawater, such as water molecules, suspended particulate matter, and colored dissolved organic matter, are prescribed based on empirical parameterizations (Mobley, 1994; Woźniak and Dera, 2007; Kirk, 2011). The effects of oil droplets on the IOPs are modeled based on the simulated oil concentration using Mie theory (Bohren and Huffman, 2008) (see more details in Appendix B). We note that the radiative transfer in the upper ocean is also strongly affected by the wavelength of the light, as shown in Appendix B. In particular, the light absorption reaches the lowest order of $O(0.01)$ m^{-1} in pure seawater around the light wavelength of 450 nm, and increases gradually to the order of $O(1)$ m^{-1} towards both the ultraviolet and infrared ends of the light spectrum; the light scattering coefficient of pure seawater decreases monotonically as the light wavelength increases (Mobley, 1994). On the other hand, both the light absorption and scattering effects induced by suspended crude oil droplets decrease monotonically as the light wavelength increases (Otremba, 2007). Therefore, a large set of simulations for a range of representative wavelengths in the full light spectrum would need to be performed in order to obtain the complete picture for the effects of the oil plumes on the upper-ocean light field. However, to avoid further complicating the simulation and data analysis, in this study we only consider the radiative transfer of the 450 nm wavelength light, which is in the spectrum range for oceanic photosynthesis. Overall, in this study we conduct simulations and data analyses for 6 cases covering two different flow conditions with three different oil droplet sizes for each. Moreover, for comparison purpose, we also conduct two benchmark cases without oil plume for both the LC and CC flow conditions.

3.2. Simulation results and statistical analysis

As shown in Fig. 5(a), for the LC condition the interaction between wave-induced Stokes drift and shear-induced turbulence is able to generate Langmuir circulations (McWilliams et al., 1997; Li et al., 2005), as indicated by the streaky structures in the vertical velocity contours (i.e. the windrows); for the CC condition, the large surface heat flux causes strong thermal instability that dominates over the weaker Craik–Leibovich second type instability caused by wave–turbulence interaction (Craik and Leibovich, 1976), and the thermal convection cells become the main flow structures as shown in Fig. 5(b). Note that the vertical velocity field in the LC case fluctuates more energetically than that in the CC case due to the effect of the Langmuir circulations, as indicated by the vertical velocity contours shown in Fig. 5. The flow field features for the wind/wave-dominant LC case and the convection-dominant CC case are consistent with those reported in the literature (e.g. McWilliams et al., 1997; Mensa et al., 2015). In response to the flow-induced transport, the surface oil plume forms different patterns due to the different characteristics of the flow conditions.

In the LC condition the oil converges into narrow downwind bands (namely the surface windrows generated by contour-rotating Langmuir cells) (McWilliams et al., 1997; Yang et al., 2014a, 2015), while in the CC condition the oil concentrates into surface patches (corresponding to convergence regions between convective cells) (Chor et al., 2018a). Moreover, as shown in Fig. 6, for the same flow condition the oil plume pattern is also strongly affected by the buoyancy of the oil droplet, which can be quantified by the floatability parameter $\beta = w_r/W$, where w_r is the droplet rise velocity due to buoyancy and W is a velocity scale representing the level of mixing induced by OML flows. For the LC condition, W can be set to be the surface Stokes drift velocity $u_{s,0}$ and $\beta = w_r/u_{s,0} = Db^{-1}$, where Db is the drift-to-buoyancy ratio proposed by Yang et al. (2014a). As shown in Fig. 6(b–d), the oil plume exhibits highly intermittent surface pattern with high local concentration in windrows when β is large and volumetrically diffused smooth pattern when β is small (Yang et al., 2014a, 2015). For the CC condition, W can be set to be the Deardorff convective velocity $w_* = (g\alpha_t\langle w'\Theta'\rangle_s z_i)^{1/3}$, where g is the gravitational acceleration, α_t is the thermal expansion

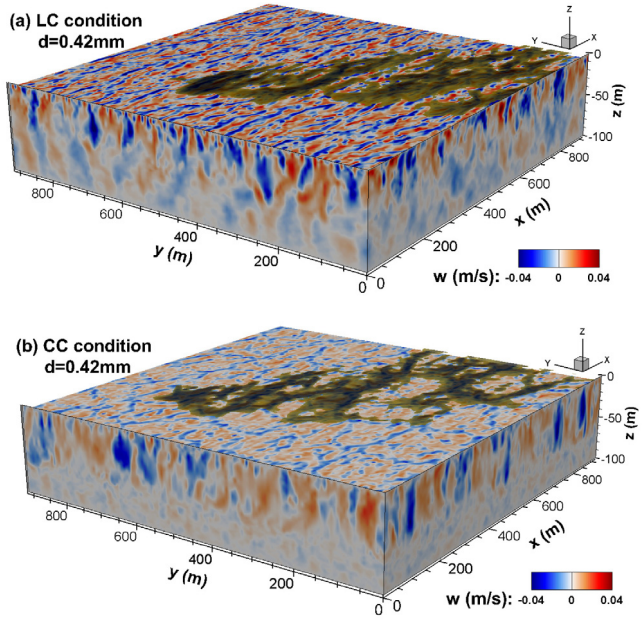

Fig. 5. Sample LES results of velocity field and surface oil plumes for the (a) LC and (b) CC conditions. The color contours denote the instantaneous vertical velocity w. The iso-surfaces of the oil concentration for $d = 0.42$ mm are also plotted, with darker color for higher oil mass concentration.

coefficient, w' is the vertical velocity fluctuation, Θ' is the temperature fluctuation, z_i is the OML depth, and $\langle\cdot\rangle_s$ denotes a Reynolds average at the surface (in practice, it is computed at the first LES grid below the mean sea surface level) (Chor et al., 2018a). It is worth mentioning that very recently, a more general form for the turbulence velocity scale W has been proposed to account for various levels of wind shear, Stokes drift, and buoyancy flux (Chor et al., 2018b).

Because the oil transport in the OML and the resulted light field variation are highly three dimensional (Fig. 1), this requires us to analyze both the horizontal and the vertical distributions of the oil concentration and their effects on the light field. Fig. 7 shows several representative instantaneous snapshots of oil concentration on the surface and the corresponding subsurface light field at 10 m depth. The vertical variations on the oil and light fields are illustrated by the vertical profiles of horizontal average statistics shown in Figs. 8 and 9. We analyze the effect of the oil on the subsurface light field by quantifying the beam attenuation coefficient c and the downward irradiance E_d (Mobley, 1994; Xu et al., 2012).

When calculating horizontal average, we focus on the flow regions contaminated by the dispersed oil plume, which can be determined statistically based on the time average of the vertically integrated oil concentration (Chen et al., 2018). Previous study has shown that the averaged oil plumes are smooth and continuous even when the instantaneous oil field is highly intermittent (Yang et al., 2015). As shown in Figs. 8(a) and 9(a), the horizontal area A of the average oil-contaminated region increases as the droplet floatability decreases. Plumes of large oil droplets possess strong floatability to overcome the downwelling motion induced by Langmuir circulations and thermal convection, forming high-concentration surface plumes that cover relatively small regions near the surface; plumes of small oil droplets have weak floatability and can be dispersed widely by OML flows over large horizontal and vertical extensions, which also dilute the local oil droplet concentration to relatively low level (Yang et al., 2014a; Chor et al., 2018a,b).

The statistics of the oil plume and light field can be obtained by performing horizontal average within A, which is denoted as $\langle\cdot\rangle_A$. As shown in Figs. 8(b) and 9(b), plumes of larger droplets tend to have

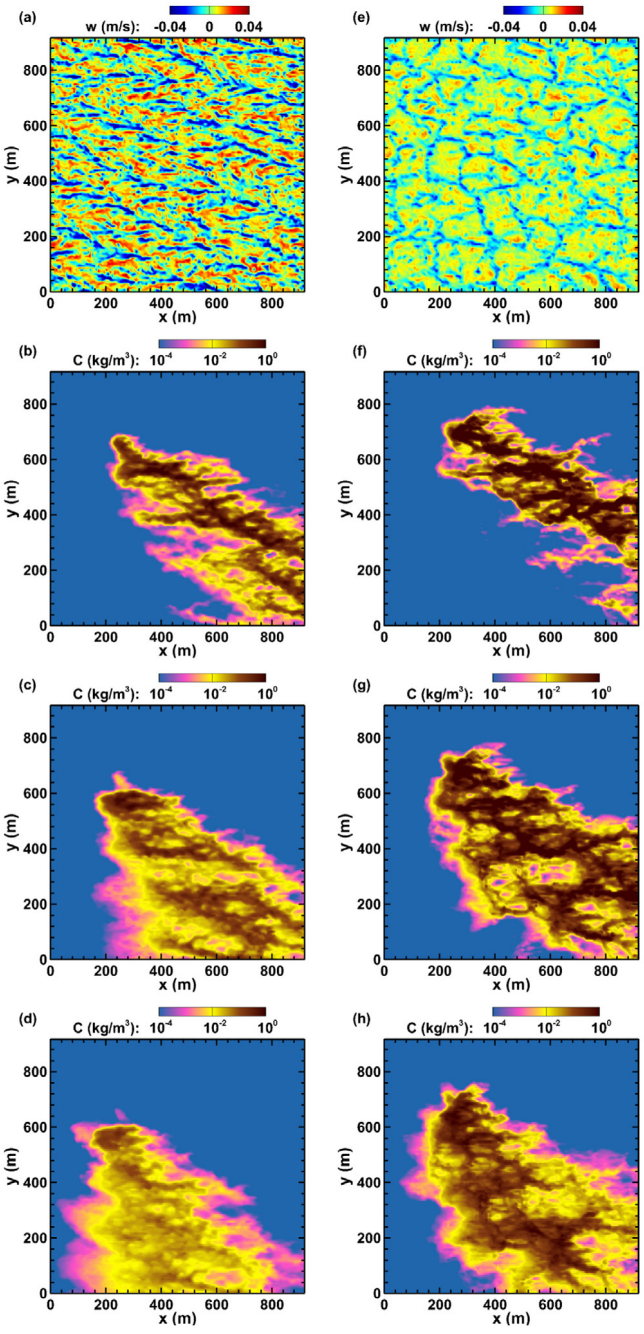

Fig. 6. Instantaneous flow and oil plume fields for LC condition (a–d) and CC condition (e–h). The panels show the contours of: (a, e) vertical velocity w on the horizontal plane at $z = -9$ m depth; and oil mass concentration C on the ocean surface ($z = 0$, m) for cases with droplet diameters of (b, f) $d = 0.70$ mm, (c, g) $d = 0.42$ mm, and (d, h) $d = 0.27$ mm.

higher average concentration near the surface with rapidly decreased concentration towards deeper depth, while plumes of smaller droplets have more smooth vertical distribution of oil concentration. As a result, the oil plumes with $d = 0.70$ mm cause significant increase of light attenuation coefficient near the surface, but this effect decreases quickly with depth due to the decrease of oil concentration (Figs. 8(b) and 9(b)). For the cases with $d = 0.42$ mm and $d = 0.27$ mm, although the increase of light attenuation coefficient near the surface may be less significant than that in the case with $d = 0.70$ mm, this effect persists over much deeper depth due to the much smoother distribution of oil droplets over the seawater column (Figs. 8(c) and 9(c)). Combining the

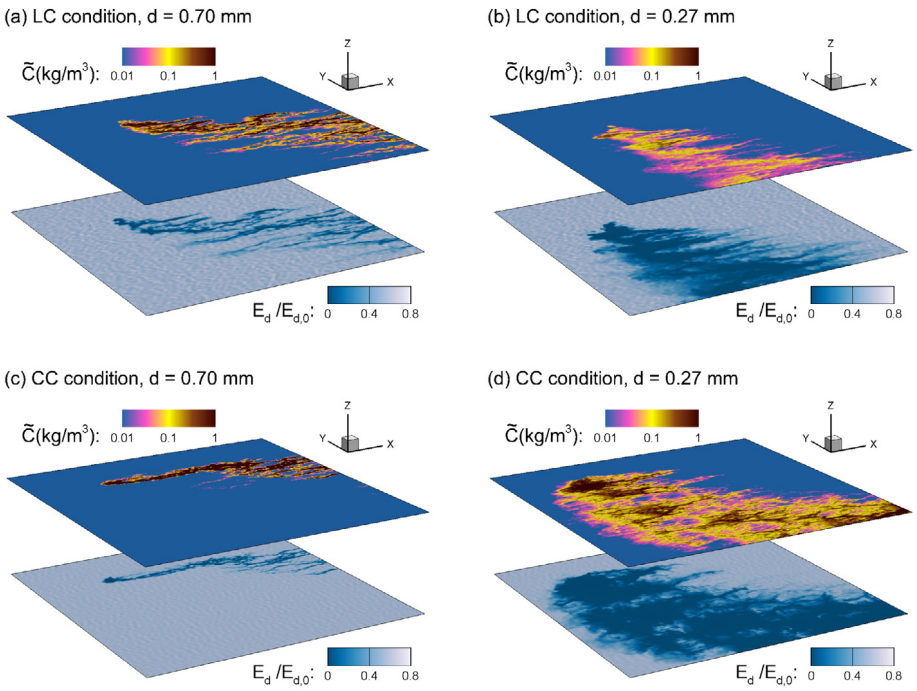

Fig. 7. Surface oil concentration (shown on the upper plane in each panel) and subsurface downward irradiance at 10 m depth (shown on the lower plane in each panel): (a) LC condition with oil droplet diameter $d = 0.70$ mm; (b) LC condition with oil droplet diameter $d = 0.27$ mm; (c) CC condition with oil droplet diameter $d = 0.70$ mm; (d) CC condition with oil droplet diameter $d = 0.27$ mm.

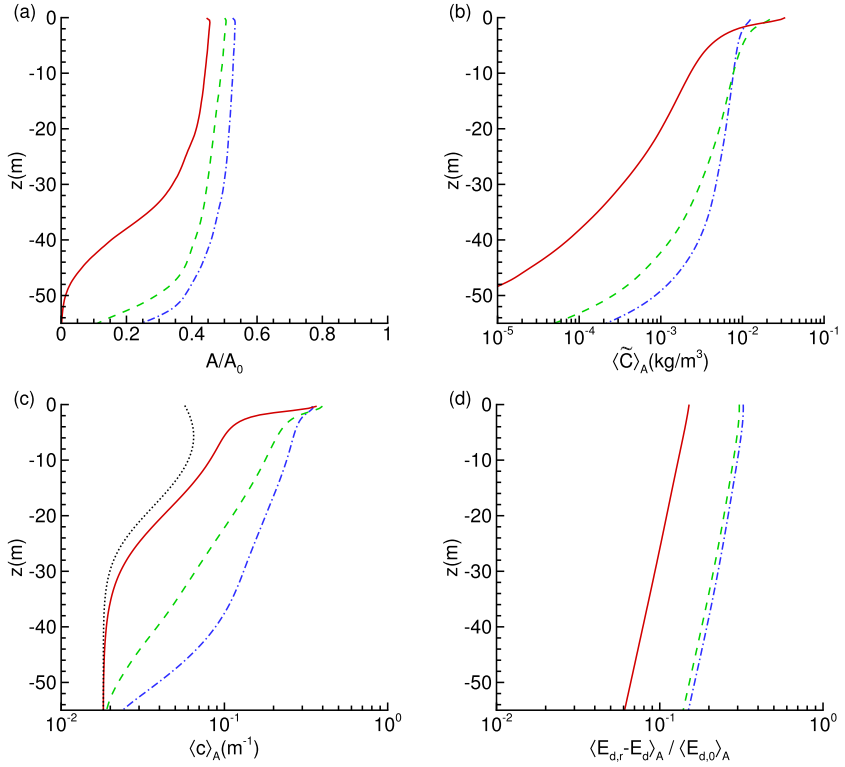

Fig. 8. Vertical profiles of horizontal average statistics for cases under the LC flow condition: (a) oil-contaminated area A (normalized by the total horizontal area A_0); (b) oil mass concentration $\langle C \rangle_A$; (c) beam attenuation coefficient $\langle c \rangle_A$; and (d) normalized deficit of downward irradiance $\langle E_{d,r} - E_d \rangle_A / \langle E_{d,0} \rangle_A$, where E_d is the downward irradiance in oil-contaminated seawater, $E_{d,r}$ is the reference downward irradiance obtained from simulation based on natural seawater, and $E_{d,0}$ is the downward irradiance of the incident light above the sea surface imposed in MCS. The results for simulation cases with different oil droplet diameters are denoted by different line patterns: solid line for $d = 0.70$ mm; dashed line for $d = 0.42$ mm; dash–dot line for $d = 0.27$ mm. In (c), the black dotted line shows the reference beam attenuation coefficient c for natural seawater.

effects of the vertical oil distribution, horizontal intermittency level of the oil plume and difference in local oil concentration (Fig. 6), the oil plumes with smaller droplets result in more significant deficit for the downward irradiance than the plumes with larger droplets, even

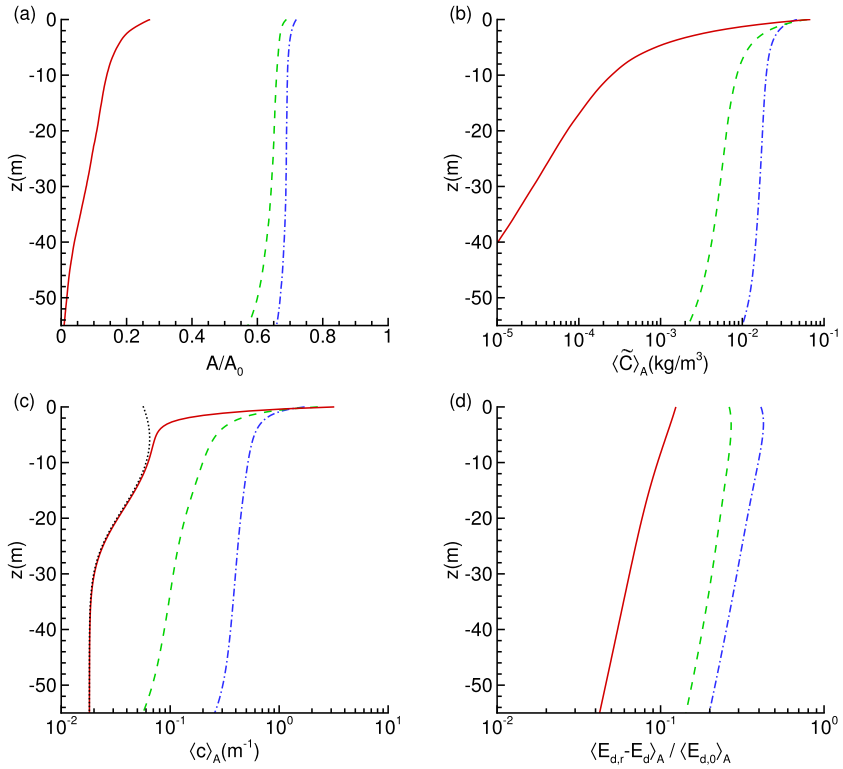

Fig. 9. Vertical profiles of horizontal average statistics for cases under the CC flow condition. The panel arrangement and line legend have the same format as in Fig. 8.

though the latter have higher local oil concentration near the surface (Figs. 8(d) and 9(d)).

It should be pointed out that the current study focuses on modeling the effects of monodispersed surface oil plumes on upper-ocean radiative transfer with idealized oceanic and oil release conditions. Separating oil plumes with different droplet sizes into different simulation cases allows us to connect the droplet size, oil plume dilution pattern and the radiative transfer. With the recent advancements on modeling oil droplet size distribution in subsea blowouts (Zhao et al., 2014, 2015; Socolofsky et al., 2015; Li et al., 2017), LES of polydispersed oil plumes can be performed to obtain in-situ modeling of more realistic surface plumes with the mixture of various droplet sizes, which will be a subject of future study. As the initial attempt, in this study we limit to the idealized setup considering the high level of complexity and computational cost involved in applying several high-fidelity numerical models.

4. Conclusion and discussion

The current study combines the strengths of several high-fidelity numerical models for simulating various physical processes (i.e. wave mechanics, oil plume dispersion by OML turbulent flows, and radiative transfer through the complex oil/seawater mixture medium) to help improve our understanding on the impact of offshore oil spills on ocean light field. Due to the high complexity of the physical processes, by no mean the current study is meant to capture all the relevant physics in this problem. Nevertheless, the simulation results presented here show that plumes of oil droplets can significantly reduce the downward irradiance of the light in the ocean euphotic zone, and this effect is strongly affected by the dynamic interaction between oil and OML flows governed by the oil droplet floatability. While in general the presence of oil plume can cause considerable reduction to the downward irradiance, this effect appears to be more significant for plumes of smaller oil droplet sizes because these plumes are dispersed more widely by the OML flows. This finding suggests that additional effect to the ocean ecosystem caused by the variation of ocean light field may need to be taken into consideration when applying dispersant for oil spill remediation and response, as dispersant can significantly reduce the oil droplet size. Moreover, it is worth mentioning that the numerical models used in this study can also be applied to simulate the backscattered light signal of surface oil plumes, which can provide useful insights to help link the remote sensing signals to the surface and subsurface characteristics of the oil plumes to support the decision making process for future oil spill response and remediation. Furhermore, even though the reduced downward irradiance obtained from the current study can be used to estimate the potential impact of oil plumes on the phytoplankton photosynthesis rate, the direct calculation of the phytoplankton population evolution and photosynthesis rate are not included in the current model. With the continuous advancement in computer power and numerical model capability, these additional features may be included into the current modeling framework. These are the subjects for future research.

Acknowledgments

This research was made possible by a grant from The Gulf of Mexico Research Initiative. D.Y. also acknowledges the financial support from start-up funds at the University of Houston. Data are publicly available through the Gulf of Mexico Research Initiative Information and Data Cooperative (GRIIDC) at https://data.gulfresearchinitiative.org/data/R5.x283.000:0004 (doi:10.7266/n7-w0hm-6f39).

Appendix A. High-order spectral simulation of sea-surface waves

In current HOS model, the continuity equation and boundary conditions (1) and (2) are solved together based on the perturbation method and pseudo-spectral method (Dommermuth and Yue, 1987). In particular, Φ is expanded into a perturbation series with respect to wave steepness to order M,

$$\Phi(x, y, z, t) = \sum_{m=1}^{M} \Phi^{(m)}(x, y, z, t) \, . \tag{A.1}$$

The surface potential Φ^s can then be expressed based on the perturbation modes $\Phi^{(m)}$ using Taylor series expansion about $z = 0$,

$$\Phi^s(x,y,t) = \sum_{m=1}^{M}\sum_{\ell=0}^{M-m}\frac{\eta^\ell}{\ell!}\frac{\partial^\ell}{\partial z^\ell}\Phi^{(m)}(x,y,z,t)\Big|_{z=0}. \tag{A.2}$$

Finally, $\Phi^{(m)}$ is rewritten into an eigenfunction expansion,

$$\Phi^{(m)}(x,y,z,t) = \sum_{n=1}^{N}\Phi_n^{(m)}(t)\Psi_n(x,y,z). \tag{A.3}$$

where $\Psi_n(x,y,z) = \exp(|\mathbf{k}(n)|z + i\mathbf{k}(n)\cdot\mathbf{x})$ is the eigenfunction under deep-water condition, $i = \sqrt{-1}$, $\mathbf{x}$ is the horizontal coordinate vector, and $\mathbf{k}(n) = (k_x(n), k_y(n))$ is the two-dimensional wavenumber vector for the nth wave mode, which is related to the scalar wavenumber as $k = |\mathbf{k}| = \sqrt{k_x^2 + k_y^2}$. By substituting Eqs. (A.1)–(A.3) into (1) and (2), the evolution equations for η and Φ^s are obtained (Dommermuth and Yue, 1987; Mei et al., 2005),

$$\frac{\partial\eta}{\partial t} = -\hat{\nabla}\eta\cdot\hat{\nabla}\Phi^s + \left(1+|\hat{\nabla}\eta|^2\right)\left[\sum_{m=1}^{M}\sum_{\ell=0}^{M-m}\frac{\eta^\ell}{\ell!}\sum_{n=1}^{N}\Phi_n^{(m)}\frac{\partial^{\ell+1}\Psi_n}{\partial z^{\ell+1}}\Big|_{z=0}\right], \tag{A.4}$$

$$\frac{\partial\Phi^s}{\partial t} = -g\eta - \frac{|\hat{\nabla}\Phi^s|^2}{2} + \frac{1+|\hat{\nabla}\eta|^2}{2}\left[\sum_{m=1}^{M}\sum_{\ell=0}^{M-m}\frac{\eta^\ell}{\ell!}\sum_{n=1}^{N}\Phi_n^{(m)}\frac{\partial^{\ell+1}\Psi_n}{\partial z^{\ell+1}}\Big|_{z=0}\right]^2. \tag{A.5}$$

In the current HOS model, Eqs. (A.4) and (A.5) are discretized using the pseudo-spectral method based on Fourier series, and integrated in time by a fourth-order Runge–Kutta scheme (Yang and Shen, 2011; Yang et al., 2013, 2014b,c).

The HOS model can capture the nonlinear wave–wave interactions and simulate an unsteady, time-resolved surface wave field. In this study, the HOS wave simulation is initialized based on the empirical wave spectra for equilibrium ocean wave conditions from Donelan and Pierson (1987) using a random phase method (Yang and Shen, 2011; Yang et al., 2014b). Under the equilibrium condition, the energy input from the wind to the wave field is weak and the HOS model may be used without the expensive coupling with a wind turbulence solver that was used in Yang and Shen (2011). As shown in Yang et al. (2013), the current HOS model can maintain the equilibrium wave spectrum well for a considerable period of time without the dynamic coupling with the wind field for energy input. Therefore, in this study the HOS model is used in a stand-alone mode to provide unsteady, time-resolved surface wave fields in spatial domain for modeling the effects of surface waves on the light refraction at the air–water interface under equilibrium wind–wave condition. Note that if a non-equilibrium wind–wave condition is to be considered, proper wind forcing should be included in the HOS model in order to capture the evolution of the wave spectrum.

We note that the study reported in the current paper mainly focuses on the simulations and analysis of the effects of the surface oil plumes on the underwater radiative transfer. The effects of sea-surface waves on the radiative transfer have already been studied extensively in previous studies (e.g., Xu et al., 2011; Xu and Yue, 2014), thus are not analyzed in detail in the current paper. It is worth mentioning that the surface wave field may also be synthesized by simple linear superposition of Fourier modes based on the empirical wave spectra, which can save the computational cost associated with simulating the wave field. However, cautions should be taken for the potential errors associated with neglecting the wave nonlinearity effects (Xu et al., 2011). Note that for the simulation cases reported in this study, the total computational cost is mostly associated with the LES modeling of the oil plume dispersion in the ocean turbulence as well as the MCS modeling of the underwater radiative transfer, and the impact of the HOS wave modeling on the computational cost is small. Therefore, in this study the HOS model is adopted for providing the surface wave field condition to the MCS considering its high-order accuracy and computational efficiency.

Appendix B. Modeling the inherent optical properties of oil contaminated seawater

In natural ocean condition, the seawater inherent optical properties vary with temperature Θ, salinity S, chlorophyll concentration C_{ch}, optical properties and number density N_d of suspended oil droplets, etc., (Mobley, 1994; Kirk, 2011), inducing significant variation to the light field (Xu et al., 2012). In the case of oil contaminated seawater, the effects of suspended crude oil droplets dominate the variation of the IOPs. In the reported simulations, the environmental parameters of natural seawater (i.e. Θ, S, and C_{ch}) are prescribed based on typical ocean environments. The instantaneous local number density of crude oil droplets is given by $N_d = C/(\rho_d\pi d^3/6)$, where C is the oil mass concentration obtained from the LES oil plume model, ρ_d is the density of oil droplet, and d is oil droplet diameter. The specific formulas used for computing the IOPs of oil-contaminated seawater are summarized below.

B.1. Modeling light absorption and scattering in natural seawater

The light absorption coefficient a can be modeled as a function of temperature Θ, salinity S, chlorophyll concentration C_{ch}, light wavelength λ_l, oil droplet diameter d and number density N_d as (Mobley, 1994; Bricaud et al., 1998; Stramski and Tegowski, 2001; Woźniak and Dera, 2007)

$$a(\Theta,S,C_{ch},d,N_d;\lambda_l) = a_w(\Theta,S;\lambda_l) + a_{SPM}(C_{ch};\lambda_l) + a_{CDOM}(C_{ch};\lambda_l) + a_d(d,N_d;\lambda_l). \tag{B.1}$$

Here, a_w represents the absorption by seawater molecules and is modeled as (Pegau et al., 1997; Jonasz and Fournier, 2007)

$$a_w(\Theta,S;\lambda_l) = a_w(\Theta_r,0;\lambda_l) + \Psi_\Theta(\Theta-\Theta_r) + \Psi_s S, \tag{B.2}$$

where Θ_r is a reference temperature, and Ψ_Θ and Ψ_s are the slope coefficients for Θ and S, respectively. Considering a representative ocean mixed layer condition with $\Theta = 20$ °C and $S = 3.5\%$, in this study we set $a_w = 0.0145$ m^{-1} (Mobley, 1994). The second term a_{SPM} represents the absorption due to suspended particulate matter (SPM) covary with the chlorophyll concentration C_{ch} (measured in mg/m^3), which can be modeled either as (Bricaud et al., 1998; Morel and Maritorena, 2001; Stramski et al., 2001; Solonenk and Mobley, 2015)

$$a_{SPM}(C_{ch};\lambda_l) = B(\lambda_l)C_{ch}^{E(\lambda_l)}, \tag{B.3}$$

or as (Haltrin, 1999; Xu et al., 2012)

$$a_{SPM}(C_{ch};\lambda_l) = a^*_{SPM}(\lambda_l)C_{ch}^{0.602}, \tag{B.4}$$

where $B(\lambda_l)$, $E(\lambda_l)$, and $a^*_{SPM}(\lambda_l)$ are empirical coefficients. The third term a_{CDOM} represents the absorption due to colored dissolved organic matter (CDOM) and can be parameterized as (Bricaud et al., 1981)

$$a_{CDOM}(C_{ch};\lambda_l) = a_{CDOM}(C_{ch};\lambda_{l,r})\exp\left[-S_{CDOM}\left(\lambda_l-\lambda_{l,r}\right)\right], \tag{B.5}$$

where $a_{CDOM}(C_{ch};\lambda_{l,r})$ depends on C_{ch}, $\lambda_{l,r}$ is a reference light wavelength, and S_{CDOM} is an empirical constant (Kirk, 2011; Solonenk and Mobley, 2015). Alternatively, a_{CDOM} can also be parameterized based on the concentrations of the first two components in CDOM (i.e. fulvic acid and humic acid) as follows (Carder et al., 1989; Haltrin, 1999; Jonasz and Fournier, 2007; Xu et al., 2012),

$$a_{CDOM}(C_{ch};\lambda_l) = C_f a^*_f\exp\left(-k_f\lambda_l\right) + C_h a^*_h\exp\left(-k_h\lambda_l\right), \tag{B.6}$$

where $C_f = 1.74098C_{ch}\exp\left(0.12327C_{ch}\right)$ is the specific concentration of fulvic acid, $a^*_f = 35.959$ m^2/mg is the specific absorption coefficient of fulvic acid, $k_f = 0.0189$ nm^{-1}, $C_h = 0.19334C_{ch}\exp\left(0.12343C_{ch}\right)$ is the specific concentration of humic acid, $a^*_h = 18.828$ m^2/mg is the specific absorption coefficient of humic acid, and $k_h = 0.01105$ nm^{-1} (Carder et al., 1989; Haltrin, 1999).

In this study, Eqs. (B.4) and (B.6) are used to model a_{SPM} and a_{CDOM}, respectively. The corresponding vertical distribution of chlorophyll concentration is prescribed based on Woźniak and Dera (2007)

$$C_{ch}(z) = C_{ch,0}\frac{C_{const} + C_m \exp[-((z+h_{max})\sigma_z)^2]}{C_{const} + C_m \exp[-(h_{max}\sigma_z)^2]}, \tag{B.7}$$

where

$$C_{const} = 10^{[-0.0437+0.8644\log C_{ch,0} - 0.0883(\log C_{ch,0})^2]}, \tag{B.8}$$

$$C_m = 0.269 + 0.245\log C_{ch,0} + 1.51(\log C_{ch,0})^2 + 2.13(\log C_{ch,0})^3 + 0.814(\log C_{ch,0})^4, \tag{B.9}$$

$$h_{max} = 17.9 - 44.6\log C_{ch,0} + 38.1(\log C_{ch,0})^2 + 1.32(\log C_{ch,0})^3 - 10.7(\log C_{ch,0})^4, \tag{B.10}$$

$$\sigma_z = 0.01\left[4.08 + 2.17\log C_{ch,0} + 0.239(\log C_{ch,0})^2 + 0.562(\log C_{ch,0})^3 + 0.514(\log C_{ch,0})^4\right], \tag{B.11}$$

and the surface concentration of chlorophyll is assumed to be $C_{ch,0} = C_{ch}(0) = 0.1$ mg/m^3 (Woźniak and Dera, 2007).

The last term a_d in Eq. (B.1) accounts for the absorption due to suspended oil droplets, which depends on the droplet number density N_d and droplet diameter d. It can be modeled based on Mie theory as (Stramski and Tegowski, 2001; Otremba and Król, 2002; Hergert and Wriedt, 2012)

$$a_d(d, N_d; \lambda_l) = (\pi d^2/4)\, Q_{ab}(d; \lambda_l)\, N_d, \tag{B.12}$$

where Q_{ab} is the absorption efficiency. Details on how to model Q_{ab} using Mie theory are given further below.

The light scattering coefficient b can be modeled as (Stramski and Tegowski, 2001; Solonenk and Mobley, 2015)

$$b(C_{ch}, d, N_d; \lambda_l) = b_w(\lambda_l) + b_{SPM}(C_{ch}; \lambda_l) + b_d(d, N_d; \lambda_l). \tag{B.13}$$

Here, b_w corresponds to the scattering caused by water molecules,

$$b_w(\lambda_l) = 5.83\times10^{-3}(\lambda_{l,r}/\lambda_l)^{4.322}; \tag{B.14}$$

b_{SPM} corresponds to the scattering caused by the SPM,

$$b_{SPM}(C_{ch}; \lambda_l) = b_s^*(\lambda_l)C_s(C_{ch}) + b_l^*(\lambda_l)C_l(C_{ch}), \tag{B.15}$$

where b_s^* (measured in m^2/mg) and C_s (measured in mg/m^3) are the specific scattering coefficient and concentration of small-size SPM, respectively, and b_l^* and C_l are the corresponding quantities for large-size SPM. They can be parameterized as (Haltrin, 1999; Solonenk and Mobley, 2015)

$$b_s^*(\lambda_l) = 1.513\times10^{-3}\left(\lambda_{l,r}/\lambda_l\right)^{1.7}, \tag{B.16}$$

$$b_l^*(\lambda_l) = 3.411\times10^{-4}\left(\lambda_{l,r}/\lambda_l\right)^{0.3}, \tag{B.17}$$

$$C_s(C_{ch}) = 17.39C_{ch}\exp\left(0.11631C_{ch}\right), \tag{B.18}$$

$$C_l(C_{ch}) = 762.84C_{ch}\exp\left(0.03092C_{ch}\right). \tag{B.19}$$

The last term b_d accounts for the scattering due to suspended oil, which can be modeled based on Mie theory as (Stramski and Tegowski, 2001; Otremba and Król, 2002; Hergert and Wriedt, 2012)

$$b_d(d, N_d; \lambda_l) = (\pi d^2/4)\, Q_{sc}(d; \lambda_l)\, N_d, \tag{B.20}$$

where Q_{sc} is the scattering efficiency. Details on how to model Q_{sc} using Mie theory are given further below.

The scattering direction is determined by the total scattering phase function, which is expressed as a weighted sum of the three contributions (Stramski and Tegowski, 2001),

$$\mathscr{B}(\Delta\theta, C_{ch}, d, N_d; \lambda_l) = \frac{\mathscr{B}_w(\Delta\theta; \lambda_l)b_w(\lambda_l)}{b(C_{ch}, d, N_d; \lambda_l)} + \frac{\mathscr{B}_{SPM}(\Delta\theta)b_{SPM}(\lambda_l)}{b(C_{ch}, d, N_d; \lambda_l)} + \frac{\mathscr{B}_d(\Delta\theta; \lambda_l)b_d(d, N_d; \lambda_l)}{b(C_{ch}, d, N_d; \lambda_l)}, \tag{B.21}$$

where $\Delta\theta$ is the relative polar angle away from the incident direction due to scattering, and $\mathscr{B}_w(\Delta\theta; \lambda_l)$, $\mathscr{B}_{SPM}(\Delta\theta)$ and $\mathscr{B}_d(\Delta\theta, \lambda_l)$ are the scattering phase functions of seawater, SPM, and other particles, respectively. Values for $\mathscr{B}_w(\Delta\theta; \lambda_l)$ can be found in Mobley (1994) and Morel and Maritorena (2001); $\mathscr{B}_{SPM}(\Delta\theta)$ is modeled by the Petzold phase function (Petzold, 1972; Stramski and Tegowski, 2001; Solonenk and Mobley, 2015); and $\mathscr{B}_d(\Delta\theta, \lambda_l)$ is modeled based on Mie theory with details given below. Note that in Eq. (B.21) the dependence on the change of azimuthal angle φ is not included by assuming homogeneity of the scattering direction with respect to φ.

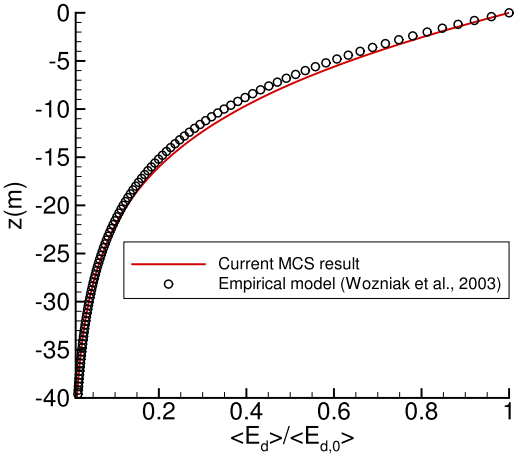

Fig. B.1. Vertical attenuation of horizontally averaged downward irradiance in seawater with a mean surface chlorophyll concentration of $C_{ch,0} = 1$ mg/m^3. The prediction based on the empirical model of Woźniak et al. (2003) is shown using the symbols and the current MCS result is shown using the solid line. In this test case, a calm sea condition is assumed so that the sea-surface is modeled to be flat.

Fig. B.1 shows the result of a MCS test case for radiative transfer of 500 nm light in a natural ocean condition (without oil) with a mean surface chlorophyll concentration of $C_{ch,0} = 1$ mg/m^3. In this test case the vertical profile of the chlorophyll concentration is modeled based on Eq. (B.7) and $C_{ch,0}$; the corresponding seawater absorption and scattering coefficients are modeled based on Eqs. (B.1) and (B.13); and the scattering phase function is modeled based on Eq. (B.21). The corresponding diffuse attenuation coefficient K_d as a function of the vertical coordinate z can be calculated based on the empirical model as (Woźniak et al., 2003; Woźniak and Dera, 2007):

$$K_d(z) = K_w + C_{ch}(z)\{C_1\exp[-a_1C_{ch}(z)] + K_{d,i}\}. \tag{B.22}$$

For the $\lambda_l = 500$ nm light, the model constants are $K_w = 0.0276$ m^{-1}, $C_1 = 0.0672$ m^2/mg, $a_1 = 0.610$ m^3/mg, and $K_{d,i} = 0.0389$ m^2/mg. Overall, the vertical profile of $\langle E_d\rangle$ obtained from the current MCS model shows good agreement with the exponential decay profile $\langle E_d\rangle(z) = \langle E_{d,0}\rangle\exp[\int_0^z K_d(\zeta)\mathrm{d}\zeta]$ predicted by the empirical model of Woźniak et al. (2003), where the K_d profile is given by Eq. (B.22).

B.2. Modeling light scattering by oil droplets based on Mie theory

The corresponding absorption and scattering coefficients of oil droplets can be calculated via Mie theory (Mie, 1908; Bohren and Huffman, 2008). In particular, the extinction efficiency Q_{ex}, scattering efficiency Q_{sc} and absorption efficiency Q_{ab} due to suspended oil droplets are calculated as (Bohren and Huffman, 2008)

$$Q_{sc} = \frac{2}{\chi^2}\sum_{n=1}^{\infty}(2n+1)(|a_n|^2 + |b_n|^2), \tag{B.23}$$

$$Q_{ex} = \frac{2}{\chi^2}\sum_{n=1}^{\infty}(2n+1)[\Re(a_n + b_n)], \tag{B.24}$$

$$Q_{ab} = Q_{ex} - Q_{sc}. \tag{B.25}$$

where $\chi = \pi d/\lambda_l$ is the diffraction parameter, $\Re(\cdot)$ is the real part of the sum of the complex numbers a_n and b_n,

$$a_n = \frac{[D_n(m\chi)/m + n/\chi]\psi_n(\chi) - \psi_{n-1}(\chi)}{[D_n(m\chi)/m + n/\chi]\xi_n(\chi) - \xi_{n-1}(\chi)}, \tag{B.26}$$

$$b_n = \frac{[D_n(m\chi)m + n/\chi]\psi_n(\chi) - \psi_{n-1}(\chi)}{[D_n(m\chi)m + n/\chi]\xi_n(\chi) - \xi_{n-1}(\chi)}, \tag{B.27}$$

$m = n_d/n_w$ is the relative refractive index, n_d is the refractive index of oil droplet, n_w is the refractive index of seawater, and $D_n(\varrho) = \mathrm{d}(\ln \psi_n(\varrho))/\mathrm{d}\varrho$ is the logarithmic derivative, which satisfies the recurrence relation

$$D_{n-1}(\varrho) = \frac{n}{\varrho} - \frac{1}{D_n(\varrho) + n/\varrho}. \tag{B.28}$$

The Riccati–Bessel functions $\psi_n(x)$ and $\xi_n(x)$ satisfy the following upward recurrence relation (Bohren and Huffman, 2008)

$$\psi_{n+1}(\chi) = \frac{2n+1}{\chi}\psi_n(\chi) - \psi_{n-1}(\chi), \tag{B.29}$$

$$\xi_{n+1}(\chi) = \frac{2n+1}{\chi}\xi_n(\chi) - \xi_{n-1}(\chi), \tag{B.30}$$

beginning with

$$\psi_0(\chi) = \sin(\chi), \tag{B.31}$$

$$\psi_{-1}(\chi) = \cos(\chi), \tag{B.32}$$

$$\xi_0(\chi) = \sin(\chi) - i\cos(\chi), \tag{B.33}$$

$$\xi_{-1}(\chi) = \cos(\chi) + i\sin(\chi), \tag{B.34}$$

where $i = \sqrt{-1}$. In this study, the complex refractive index of spherical oil droplet is set to be $n_d = 1.494 + 0.0089\,i$ for light with wavelength $\lambda_l = 450$ nm (Otremba and Piskozub, 2004), and the refractive index of seawater is $n_w = 1.34$.

The scattering function due to oil droplets can also be determined based on a_n and b_n as (Fu and Sun, 2001; Bohren and Huffman, 2008)

$$P_d(\Delta\theta) = \frac{2}{\chi^2 Q_{sc}}(|S_1(\Delta\theta)|^2 + |S_2(\Delta\theta)|^2), \tag{B.35}$$

where S_1 and S_2 are the amplitude functions,

$$S_1(\Delta\theta) = \sum_{n=1}^{\infty}\frac{2n+1}{n(n+1)}[a_n\pi_n(\cos\Delta\theta) + b_n\tau_n(\cos\Delta\theta)], \tag{B.36}$$

$$S_2(\Delta\theta) = \sum_{n=1}^{\infty}\frac{2n+1}{n(n+1)}[a_n\tau_n(\cos\Delta\theta) + b_n\pi_n(\cos\Delta\theta)]. \tag{B.37}$$

Here, the angular functions π_n and τ_n are defined as $\pi_n = P_n^1/\sin\Delta\theta$ and $\tau_n = \mathrm{d}P_n^1/\mathrm{d}(\Delta\theta)$, where P_n^1 are the associated Legendre functions of the first kind of degree n and order 1. In the simulation, π_n and τ_n can be calculated based on the following upward recurrence relations (Bohren and Huffman, 2008),

$$\pi_n(\varsigma) = \frac{2n-1}{n-1}\varsigma\pi_{n-1}(\varsigma) - \frac{n}{n-1}\pi_{n-2}(\varsigma), \tag{B.38}$$

$$\tau_n(\varsigma) = n\varsigma\pi_n(\varsigma) - (n+1)\pi_{n-1}(\varsigma), \tag{B.39}$$

beginning with

$$\pi_1(\varsigma) = 1, \tag{B.40}$$

$$\pi_0(\varsigma) = 0, \tag{B.41}$$

where $\varsigma = \cos\Delta\theta$. The scattering phase function used in Eq. (B.21) can then be obtained as $\mathscr{B}_d = P_d/4\pi$.

Fig. B.2 shows some sample results for the scattering phase functions for various diffraction parameters obtained using Mie theory. The results computed by Mie theory scattering module in the current MCS model are plotted together with the theoretical results from Fu and Sun (2001). Note that the values from Fu and Sun (2001) are reproduced by digitalizing the results reported in their Fig. 5, so some small artificial errors may be induced during this image digitalization process. Nevertheless, Fig. B.2 shows good agreement between the two independent calculations, which shows that the Mie scattering model is implemented correctly in the current MCS model framework.

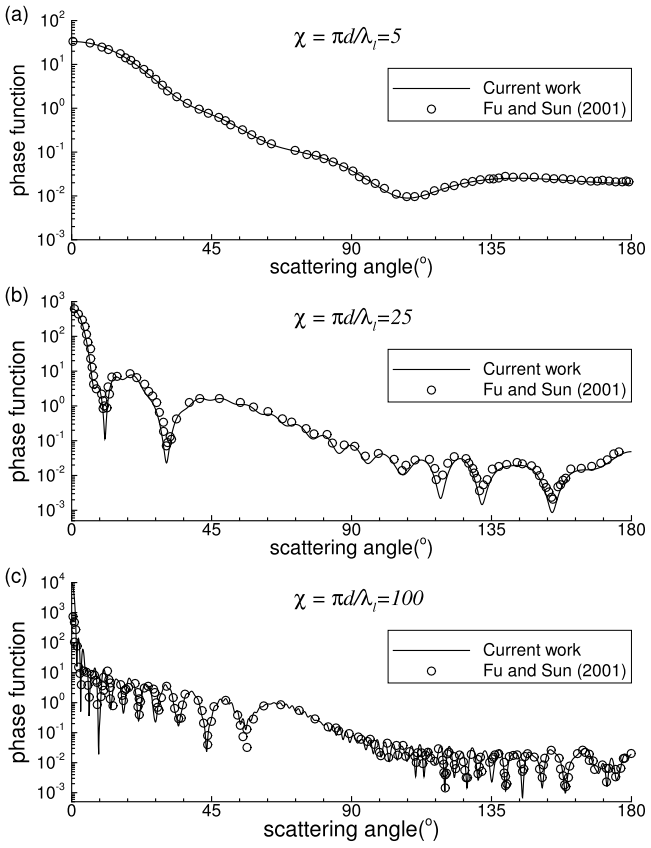

Fig. B.2. Scattering phase function as a function of the scattering angle for spherical particles with diffraction parameters: (a) $\chi = 5$; (b) $\chi = 25$; (c) $\chi = 100$. For the calculation shown in this figure, the particle's refractive index is set to be $n_d = 1.0$ and the medium's refractive index is set to be 1.34. The values calculated by Mie theory module in the current MCS model are shown by the solid lines, and the values reported by Fu and Sun (2001) (also based on Mie theory) are shown by the symbols.

It should be noted that Mie theory may not always provide accurate prediction of the volume scattering functions for nonspherical particles. The oil droplets dispersed in the upper ocean boundary layer may exhibit noticeable deformations due to the forcing induced by the oceanic flows (such as turbulence and waves), which has not been well studied due to the complex physical processes involved. Moreover, to the best of the authors' knowledge, up to date there is no reliable and accurate empirical models for the volume scattering functions of oil–seawater mixture in a dynamic ocean environment. Like what is pointed out by Bohren and Huffman (2008), for the complex problem studied in this paper, Mie theory seems to be one of the only few feasible methods for modeling the light-scattering properties of the oil-contaminated seawater. However, if new advancements are made in the future on the empirical or theoretical modeling of the effects of oil droplets on light scattering, the current MCS model can be readily improved by implementing these new scattering models to replace the existing Mie theory module.

B.3. Light refraction at the air–water interface

When an unpolarized light enters the water through the air–water interface, the refraction follows the Snell's law (Mobley, 1994):

$$n_a\sin(\gamma_i) = n_w\sin(\gamma_t), \tag{B.42}$$

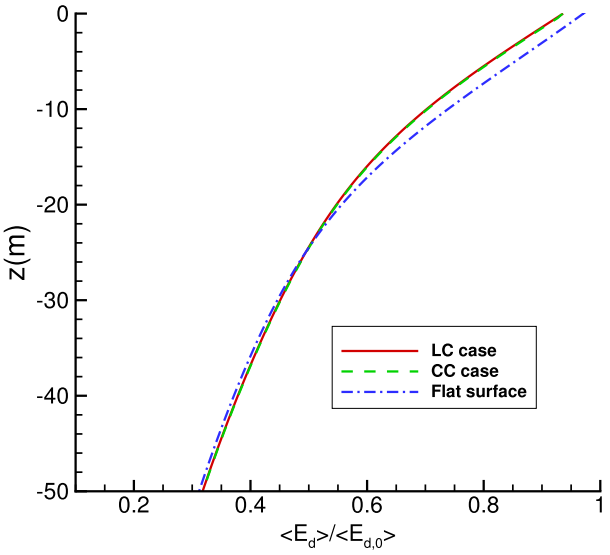

Fig. B.3. Vertical profiles of horizontally averaged downward irradiance $\langle E_d \rangle$ in the seawater without oil plumes. The profiles are normalized by the reference value of the incident light $\langle E_{d,0} \rangle$ at the sea surface.

where γ_i is the incident angle with respect to the interface normal direction, γ_t is the transmitted angle on the water side, and n_a and n_w are the optical refractive indices of air and water, respectively. The reflectance r of the radiant energy is given by the Fresnel equations (Mobley, 1994):

$$r = \begin{cases} \frac{1}{2}\left\{ \left[\frac{\sin(\gamma_i - \gamma_t)}{\sin(\gamma_i + \gamma_t)}\right]^2 + \left[\frac{\tan(\gamma_i - \gamma_t)}{\tan(\gamma_i + \gamma_t)}\right]^2 \right\}, & \text{if } \gamma_i \neq 0, \\ \left(\frac{n_a - n_w}{n_a + n_w}\right)^2, & \text{if } \gamma_i = 0. \end{cases} \tag{B.43}$$

In the MCS model, for a photon packet passing the air–water interface, the refraction of its trajectory is modeled based on Eq. (B.42) and the transmitted energy that the photon packet carries into the water is $E_t = E_i(1 - r)$, where E_i is the incident energy of the photon packet and r is determined by Eq. (B.43) (Leathers et al., 2004).

Fig. B.3 shows the downward irradiance E_d in the seawater without oil plumes for the LC and CC cases. For comparison, an additional reference case with a flat sea surface is also shown. This figure illustrates the effect of sea-surface waves for the downward irradiance shown in Figs. 8 and 9. The presence of the sea-surface wave field causes a small fraction of the incident light energy to reflect back to the air, resulting smaller downward irradiance under the wave surface than that under the flat water surface (corresponding to the idealized calm-sea condition). Note that the wave fields in the LC and CC cases obey the same empirical wave spectrum model from Donelan and Pierson (1987). Although the peak wavelengths of sea-surface waves in these two cases are different (see Section 3.1), the surface slopes of the waves in the high wavenumber range are similar between the two cases, resulting in similar initial downward irradiance underneath the wave surface. The downward irradiances for the LC and CC cases obtained without oil plumes are used as the reference value $E_{d,r}$ in Figs. 8(d) and 9(d) for obtaining the oil-induced deficit.

References

Alam, M.-R., Liu, Y., Yue, D.K.P., 2010. Oblique sub- and super-harmonic Bragg resonance of surface waves by bottom ripples. J. Fluid Mech. 643, 437–447.

Antonopoulos-Domis, M., 1981. Large-eddy simulation of a passive scalar in isotropic turbulence. J. Fluid Mech. 104, 55–79.

Atlas, R.M., Hazen, T.C., 2011. Oil biodegradation and bioremediation: a tale of the two worst spills in US history. Environ. Sci. Technol. 45, 6709–6715.

Bacosa, H.P., Erdner, D.L., Liu, Z., 2015. Differentiating the roles of photooxidation and biodegradation in the weathering of Light Louisiana Sweet crude oil in surface water from the Deepwater Horizon site. Mar. Pollut. Bull. 95 (1), 265–272.

Balachandar, S., Eaton, J.K., 2010. Turbulent dispersed multiphase flow. Annu. Rev. Fluid Mech. 42, 111–133.

Bohren, C.F., Huffman, D.R., 2008. Absorption and Scattering of Light by Small Particles. John Wiley and Sons Ltd.

Bou-Zeid, E., Meneveau, C., Parlange, M.B., 2005. A scale-dependent Lagrangian dynamic model for large eddy simulation of complex turbulent flows. Phys. Fluids 17, 025105.

Bricaud, A., Morel, A., Babin, M., Allali, K., Claustre, H., 1998. Variations of light absorption by suspended particles with chlorophyll a concentration in oceanic (case 1) waters: Analysis and implications for bio-optical models. J. Geophys. Res. 103, 31033–31044.

Bricaud, A., Morel, A., Prieur, L., 1981. Absorption by dissolved organic matter of the sea (yellow substance) in the UV and visible domains. Limnol. Oceanogr. 26, 43–53.

Camilli, R., Reddy, C.M., Yoerger, D.R., Van Mooy, B.A.S., Jakuba, M.V., Kinsey, J.C., McIntyre, C.P., Sylva, S.P., Maloney, J.V., 2010. Tracking hydrocarbon plume transport and biodegradation at Deepwater Horizon. Science 330, 201–204.

Carder, K.L., Stewart, R.G., Harvey, G.R., Ortner, P.B., 1989. Marine humic and fulvic acids: their effects on remote sensing of ocean chlorophyll. Limnol. Oceanogr. 34, 68–81.

Chamecki, M., Meneveau, C., Parlange, M., 2008. A hybrid spectral/finite-volume algorithm for large-eddy simulation of scalars in the atmospheric boundary layer. Boundary-Layer Meteorol. 128, 473–484.

Chamecki, M., Meneveau, C., Parlange, M., 2009. Large eddy simulation of pollen transport in the atmospheric boundary layer. J. Aerosol Sci. 40, 241–255.

Chen, B., Yang, D., Meneveau, C., Chamecki, M., 2016. Effects of swell on transport and dispersion of oil plumes within the ocean mixed layer. J. Geophys. Res. Oceans 121, 3564–3578.

Chen, B., Yang, D., Meneveau, C., Chamecki, M., 2018. Numerical study of the effects of chemical dispersant on oil transport from an idealized underwater blowout. Phys. Rev. Fluids 3, 083801.

Chor, T., Yang, D., Meneveau, C., Chamecki, M., 2018a. Preferential concentration of noninertial buoyant particles in the ocean mixed layer under free convection. Phys. Rev. Fluids 3, 064501.

Chor, T., Yang, D., Meneveau, C., Chamecki, M., 2018b. A turbulence velocity scale for predicting the fate of buoyant materials in the oceanic mixed layer. Geophys. Res. Lett. 45, 11817–11826.

Clift, R., Grace, J.R., Weber, M.E., 1978. Bubbles, Drops, and Particles. Academic, New York.

Craik, A.D.D., Leibovich, S., 1976. A rational model for Langmuir circulations. J. Fluid Mech. 73, 401–426.

D'Asaro, E.A., 2014. Turbulence in the upper-ocean mixed layer. Annu. Rev. Mar. Sci. 6, 101–115.

Dommermuth, D.G., Yue, D.K.P., 1987. A high-order spectral method for the study of nonlinear gravity waves. J. Fluid Mech. 184, 267–288.

Donelan, M.A., 1982. The dependence of the aerodynamic drag coefficient on wave parameters. In: Proceedings of the First International Conference on Meteorology and Air Sea Interaction of the Coastal Zone. American Meteorological Society, Boston, MA, pp. 381–387.

Donelan, M.A., Pierson, W.J., 1987. Radar scattering and equilibrium ranges in wind-generated waves with application to scatterometry. J. Geophys. Res. Oceans 92, 4971–5029.

Edson, J., Crawford, T., Crescenti, J., Farrar, T., Frew, N., Gerbi, G., Helmis, C., Hristov, T., Khelif, D., Jessup, A., Jonsson, H., Li, M., Mahrt, L., McGillis, W., Plueddemann, A., Shen, L., Skyllingstad, E., Stanton, T., Sullivan, P., Sun, J., Trowbridge, J., Vickers, D., Wang, S., Wang, Q., Weller, R., Wilkin, J., Williams, III, A.J., Yue, D.K.P., Zappa, C., 2007. The coupled boundary layers and air-sea transfer experiment in low winds. Bull. Amer. Meteor. Soc. 88, 341–356.

Ferry, J., Balachandar, S., 2001. A fast Eulerian method for disperse two-phase flow. Int. J. Multiph. Flow. 27, 1199–1226.

Fu, Q., Sun, W., 2001. Mie theory for light scattering by a spherical particle in an absorbing medium. Appl. Opt. 40, 1354–1361.

Gordon, H.R., 1985. Ship perturbation of irradiance measurements at sea. 1. Monte–Carlo simulations. Appl. Opt. 24, 4172–4182.

Goullet, A., Choi, W., 2011. A numerical and experimental study on the nonlinear evolution of long-crested irregular waves. Phys. Fluids 23, 016601.

Grant, A.L.M., Belcher, S.E., 2009. Characteristics of Langmuir turbulence in the ocean mixed layer. J. Phys. Oceanogr. 39, 1871–1887.

Haltrin, V.I., 1999. Chlorophyll-based model of seawater optical properties. Appl. Opt. 38, 6826–6832.

Harcourt, R.R., D'Asaro, E.A., 2008. Large-eddy simulation of Langmuir turbulence in pure wind seas. J. Phys. Oceanogr. 38, 1542–1562.

Hazen, T.C., Dubinsky, E.A., DeSantis, T.Z., Andersen, G.L., Piceno, Y.M., Singh, N., Jansson, J.K., Probst, A., Borglin, S.E., Fortney, J.L., Stringfellow, W.T., Bill, M., Conrad, M.E., Tom, L.M., Chavarria, K.L., Alusi, T.R., Lamendella, R., Joyner, D.C., Spier, C., Baelum, J., Auer, M., Zemla, M.L., Chakraborty, R., Sonnenthal, E.L., D?haeseleer, P., Holman, H.-Y.N., Osman, S., Lu, Z., Van Nostrand, J.D., Deng, Y., Zhou, J., Mason, O.U., 2010. Deep-sea oil plume enriches indigenous oil-degrading bacteria. Science 330, 204–208.

Hergert, W., Wriedt, T. (Eds.), 2012. The Mie Theory: Basics and Applications. Springer.
Jonasz, M., Fournier, G.R., 2007. Light Scattering by Particles in Water: Theoretical and Experimental Foundations. Elsevier.
King, S.M., Leaf, P.A., Olson, A.C., Ray, P.Z., Tarr, M.A., 2014. Photolytic and photocatalytic degradation of surface oil from the Deepwater Horizon spill. Chemosphere 95, 415–422.
Kirk, J.T.O., 1981a. Monte–Carlo procedure for simulating the penetration of light into natural waters. Theor. Appl. Genet. 60, 197–214.
Kirk, J.T.O., 1981b. Monte–Carlo study of the nature of the underwater light field in, and the relationships between optical-properties of, turbid yellow waters. Aust. J. Marine. Freshwater Res. 32, 517–532.
Kirk, J.T., 2011. Light and Photosynthesis in Aquatic Ecosystems, third ed. Cambridge University Press.
Król, T., Stelmaszewski, A., Freda, W., 2006. Variability in the optical properties of a crude oil–seawater emulsion. Oceanologia 48, 203–211.
Kukulka, T., Law, K.L., Proskurowski, G., 2016. Evidence for the influence of surface heat fluxes on turbulent mixing of microplastic marine debris. J. Phys. Oceanogr. 46, 809–815.
Kukulka, T., Plueddemann, A.J., Trowbridge, J.H., Sullivan, P.P., 2009. Significance of Langmuir circulation in upper ocean mixing: Comparison of observations and simulations. Geophys. Res. Lett. 36, L10603.
Kukulka, T., Plueddemann, A.J., Trowbridge, J.H., Sullivan, P.P., 2010. Rapid mixed layer deepening by the combination of Langmuir and shear instabilities: A case study. J. Phys. Oceanogr. 40, 2381–2400.
Kumar, V., Kleissl, J., Meneveau, C., Parlange, M., 2006. Large-eddy simulation of a diurnal cycle in the turbulent atmospheric boundary layer: Atmospheric stability and scaling issue. Water Resour. Res. 42, W06D09.
Lay, C.R., Morris, J.M., Takeshita, R., Forth, H.P., Travers, C.L., Roberts, A.P., Alloy, M., Garner, T.R., Bridges, K., 2015. Incident Ultraviolet (UV) Radiation and Extinction Coefficients in the Northern Gulf of Mexico During the Deepwater Horizon Oil Spill, DWH Toxicity NRDA Technical Working Group Report (TOX_TR.06), Boulder, CO.
Leathers, R.A., Downes, T.V., Davis, C.O., Mobley, C.D., 2004. Monte–Carlo Radiative Transfer Simulations for Ocean Optics: A Practical Guide. Tech. Rep. NRL/MR/5660–04-8819, Naval Research Laboratory.
Lee, Z.-P., Du, K.-P., Arnone, R., 2005. A model for the diffuse attenuation coefficient of downwelling irradiance. J. Geophys. Res. 110, C02016.
Leibovich, S., 1983. The form and dynamics of Langmuir circulation. Annu. Rev. Fluid Mech. 15, 391–427.
Li, Q., Fox-Kemper, B., 2017. Assessing the effects of Langmuir turbulence on the entrainment buoyancy flux in the ocean surface boundary layer. J. Phys. Oceanogr. 47, 2863–2886.
Li, M., Garrett, C., Skyllingstad, E., 2005. A regime diagram for classifying turbulent large eddies in the upper ocean. Deep-Sea Res. I 52, 259–278.
Li, Z., Spaulding, M., French McCay, D., Crowley, D., Payne, J.R., 2017. Development of a unified oil droplet size distribution model with application to surface breaking waves and subsea blowout releases considering dispersant effects. Mar. Pollut. Bull. 114, 247–257.
Lilly, D.K., 1967. The representation of small-scale turbulence in numerical simulation experiments. In: Goldstein, H.H. (Ed.), Proceedings of the IBM Scientific Computing Symposium on Environmental Science, pp. 195–210.
Liu, Y., Yue, D.K.P., 1998. On generalized Bragg scattering of surface waves by bottom ripples. J. Fluid Mech. 356, 297–326.
Mason, P., 1989. Large-eddy simulation of the convective atmospheric boundary layer. J. Atmos. Sci. 46, 1492–1516.
McWilliams, J.C., Restrepo, J.M., 1999. The wave-driven ocean circulation. J. Phys. Oceanogr. 29, 2523–2540.
McWilliams, J.C., Sullivan, P.P., 2000. Vertical mixing by Langmuir circulation. Spill Sci. Technol. Bull. 6 (3–4), 225–237.
McWilliams, J.C., Sullivan, P.P., Moeng, C.-H., 1997. Langmuir turbulence in the ocean. J. Fluid Mech. 334, 1–30.
Mei, C.C., Stiassnie, M., Yue, D.K.P., 2005. Theory and Applications of Ocean Surface Waves. Part 2: Nonlinear Aspects. World Scientific.
Mensa, J.A., Özgökmen, T.M., Poje, A.C., Imberger, J., 2015. Material transport in a convective surface mixed layer under weak wind forcing. Ocean Model. 96, 226–242.
Mie, G., 1908. Beiträge zur Optik trüber Medien, speziell kolloidaler Metallüsungen. Ann. Phys. 330, 377–445.
Mobley, C.D., 1994. Light and Water: Radiative Transfer in Natural Waters. Academic Press.
Moeng, C.-H., 1984. A large-eddy simulation model for the study of planetary boundary-layer turbulence. J. Atmos. Sci. 6, 2311–2330.
Morel, A., Maritorena, S., 2001. Bio-optical properties of oceanic waters: a reappraisal. J. Geophys. Res. 106, 7163–7180.
Noh, Y., Kang, I.S., Herold, M., Raasch, S., 2006. Large eddy simulation of particle settling in the ocean mixed layer. Phys. Fluids 18, 085109.
Otremba, Z., 2007. Oil droplets as light absorbents in seawater. Opt. Express 15, 8592–8597.
Otremba, Z., Król, T., 2002. Modeling of the crude oil suspension impact on inherent optical parameters of coastal seawater. Pol. J. Environ. Stud. 11, 407–411.
Otremba, Z., Piskozub, J., 2004. Phase functions of oil-in-water emulsions. Opt. Appl. XXXIV, 93–99.
Özgökmen, T.M., Poje, A.C., Fischer, P.F., Childs, H., Krishnan, H., Garth, C., Haza, A.C., Ryan, E., 2012. On multi-scale dispersion under the influence of surface mixed layer instabilities and deep flows. Ocean Model. 56, 16–30.
Özgökmen, T.M., Poje, A.C., Fischer, P.F., Haza, A.C., 2011. Large eddy simulations of mixed layer instabilities and sampling strategies. Ocean Model. 39, 311–331.
Pegau, W.S., Gray, D., Zaneveld, J.R.V., 1997. Absorption and attenuation of visible and near-infrared light in water: dependence on temperature and salinity. Appl. Opt. 36, 6035–6046.
Petzold, T.J., 1972. Volume Scattering Functions for Selected Ocean Waters. Tech. Rep., Scripps Institution of Oceanography, Naval Air Development Center.
Plass, G.N., Kattawar, G.W., 1972. Monte–Carlo calculations of radiative transfer in the Earth's atmosphere–ocean system: I Flux in the atmosphere and ocean. J. Phys. Oceanogr. 8, 139–145.
Polton, J.A., Smith, J.A., MacKinnon, J.A., Tejada-Martinez, A.E., 2008. Rapid generation of high-frequency internal waves beneath a wind and wave forced oceanic surface mixed layer. Geophys. Res. Lett. 35, L13602.
Radović, J.R., Aeppli, C., Nelson, R.K., Jimenez, N., Reddy, C.M., Bayona, J.M., Albaigés, J., 2014. Assessment of photochemical processes in marine oil spill fingerprinting. Mar. Pollut. Bull. 79 (1–2), 268–277.
Ray, P.Z., Chen, H., Podgorski, D.C., McKenna, A.M., Tarr, M.A., 2014. Sunlight creates oxygenated species in water-soluble fractions of Deepwater Horizon oil. J. Hazardous Mater. 280, 636–643.
Rudź, K., Darecki, M., Toczek, H., 2013. Modelling the influence of oil content on optical properties of seawater in the Baltic Sea. J. Europ. Opt. Soc. Rap. Publ. 8, 13063.
Skyllingstad, E.D., Denbo, D.W., 1995. An ocean large-eddy simulation of Langmuir circulations and convection in the surface mixed layer. J. Geophys. Res. 100, 8501–8522.
Smagorinsky, J., 1963. General circulation experiments with the primitive equations I: The basic experiment. Mon. Weather Rev. 91, 99–164.
Smith, R.C., Baker, K.S., 1981. Optical properties of the clearest natural waters (200–800 nm). Appl. Opt. 20, 177–184.
Socolofsky, S.A., Adams, E.E., Boufadel, M.C., Aman, Z.M., Johansen, Ø., Konkel, W.J., Lindo, D., Madsen, M.N., North, E.W., Paris, C.B., Rasmussen, D., Reed, M., Rønningen, P., Sim, L.H., Uhrenholdt, T., Anderson, K.G., Cooper, C., Nedwed, T.J., 2015. Intercomparison of oil spill prediction models for accidental blowout scenarios with and without subsea chemical dispersant injection. Mar. Pollut. Bull. 96, 110–126.
Solonenk, M.G., Mobley, C.D., 2015. Inherent optical properties of Jerlov water types. Appl. Opt. 54, 5392–5401.
Stramski, D., Bricaud, A., Morel, A., 2001. Modeling the inherent optical properties of the ocean based on the detailed composition of the planktonic community. Appl. Opt. 40, 2929–2945.
Stramski, D., Tegowski, J., 2001. Effects of intermittent entrainment of air bubbles by breaking wind waves on ocean reflectance and underwater light field. J. Geophys. Res. 106, 31345–31360.
Sullivan, P.P., McWilliams, J.C., 2010. Dynamics of winds and currents coupled to surface waves. Annu. Rev. Fluid Mech. 42, 19–42.
Sullivan, P.P., McWilliams, J.C., Moeng, C.-H., 1994. A subgrid-scale model for LES of planetary boundary layer flows. Bound.-Layer Meteorol. 71, 247–276.
Tanaka, M., 2001. Verification of Hasselmann's energy transfer among surface gravity waves by direct numerical simulations of primitive equations. J. Fluid Mech. 444, 199–221.
Wang, L., Jacques, S.L., Zheng, L., 1995. MCML–Monte–Carlo modeling of light transport in multi-layered tissues. Comput. Methods Programs Biomed. 47, 131–146.
Wang, X., Wang, L.V., 2002. Propagation of polarized light in birefringent turbid media: A Monte–Carlo study. J. Biomed. Opt. 7, 279–290.
Webb, A., Fox-Kemper, B., 2011. Wave spectral moments and Stokes drift estimation. Ocean Model. 40, 273–288.
Woźniak, B., Dera, J., 2007. Light Absorption in Sea Water. Springer.
Woźniak, B., Dera, J., Ficek, D., Majchrowski, R., Ostrowska, M., Kaczmarek, S., 2003. Modelling light and photosynthesis in the marine environment. Oceanologia 45, 171–245.
Xu, Z., Guo, X., Shen, L., Yue, D.K.P., 2012. Radiative transfer in ocean turbulence and its effect on underwater light field. J. Geophys. Res. 117, C00H18.
Xu, Z., Yue, D.K.P., 2014. Monte–Carlo radiative transfer simulation for the near-ocean-surface high-resolution downwelling irradiance statistics. Opt. Eng. 53, 051408.
Xu, Z., Yue, D.K.P., Shen, L., Voss, K.J., 2011. Patterns and statistics of in-water polarization under conditions of linear and nonlinear ocean surface waves. J. Geophys. Res. 116, C00H12.
Yang, D., Chamecki, M., Meneveau, C., 2014a. Inhibition of oil plume dilution in Langmuir ocean circulation. Geophys. Res. Lett. 41, 1632–1638.
Yang, D., Chen, B., Chamecki, M., Meneveau, C., 2015. Oil plumes and dispersion in langmuir, upper-ocean turbulence: Large-eddy simulations and K-profile parameterization. J. Geophys. Res. Oceans 120, 4729–4759.
Yang, D., Chen, B., Socolofsky, S., Chamecki, M., Meneveau, C., 2016. Large-eddy simulation and parameterization of buoyant plume dynamics in stratified flow. J. Fluid Mech. 794, 798–833.

Yang, D., Meneveau, C., Shen, L., 2013. Dynamic modeling of sea-surface roughness for large-eddy simulation of wind over ocean wavefield. J. Fluid Mech. 726, 62–99.
Yang, D., Meneveau, C., Shen, L., 2014b. Large-eddy simulation of offshore wind farm. Phys. Fluids 26, 025101.
Yang, D., Meneveau, C., Shen, L., 2014c. Effect of downwind swells on offshore wind energy harvesting – A large-eddy simulation study. Renew. Energy 70, 11–23.
Yang, D., Shen, L., 2011. Simulation of viscous flows with undulatory boundaries. Part II: Coupling with other solvers for two-fluid computations. J. Comput. Phys. 230, 5510–5531.
You, Y., Zhai, P.-W., Kattawar, G.W., Yang, P., 2009. Polarized radiance fields under a dynamic ocean surface: a three-dimensional radiative transfer solution. Appl. Opt. 48, 3019–3029.
Zakharov, V.E., 1968. Stability of periodic waves of finite amplitude on the surface of a deep fluid. J. Appl. Mech. Tech. Phys. 2, 190–194.
Zhao, L., Boufadel, M.C., Adams, E., Socolofsky, S.A., King, T., Lee, K., Nedwed, T., 2015. Simulation of scenarios of oil droplet formation from the Deepwater horizon blowout. Mar. Pollut. Bull. 101, 304–319.
Zhao, L., Boufadel, M.C., Socolofsky, S.A., Adams, E., King, T., Lee, K., 2014. Evolution of droplets in subsea oil and gas blowouts: development and validation of the numerical model VDROP-J. Mar. Pollut. Bull. 83, 58–69.
Zheng, L., Yapa, P.D., 2000. Buoyant velocity of spherical and nonspherical bubbles/droplets. J. Hydraul. Eng. 126, 852–854.